Composition Analysis of High-T_c Superconducting Thin Films By Quantitative X-Ray Fluorescence

by

Tareg Elsahlli, B. Sc.

A Thesis
submitted to the Department of Physics
in partial fulfillment of the requirements
for the degree of
Master of Science

August 1992
Brock University
St. Catharines, Ontario

Acknowledgments

I would like to thank Dr. Moore for giving me the opportunity to work with him and for his support, encouragement, and patience throughout the project. Also I would like to thank Dr. Koffyberg and Dr. Zalaski for their help.

Abstract

A method is presented for determining the composition of thin films containing the elements Bi, Sr, Br, Cu, and Ca. Quantitative x-ray fluorescence (XRF) consisting of radioactive sources (secondary foil excitor ^{241}Am-Mo source and ^{55}Fe source), a Si(Li) detector, and a multichannel analyzer were employed. The XRF system was calibrated by using sol gel thin films of known element composition and also by sputtered thin films analyzed by the conventional Rutherford Back Scattering (RBS). The XRF system has been used to assist and optimize the sputter target composition required to produce high-T_c BiSrCaCuO films with the desired metal composition.

Contents

List of Tables

List of Figures

(1) Introduction

Thin films in the broadest sense of the term have been known to mankind for hundreds and possibly thousands of years. Examples that come to mind are the layers of paint used by pre-historic man to decorate caves and, comparatively recently, some of the decorative glazes that were applied to primitive pottery. However, today thin film technology normally refers to films deposited on a substrate in a controlled way, often by some type of atom by atom process [1].

Scientists are interested in thin films, because of their many useful applications and their properties and because they may possess physical properties (mechanical, electronic, optical) which are different from those of the bulk material [1,2].

Thin films have many applications in various fields, including electronics and optical devices. High-T_c superconducting thin films are being applied to the development of, for example, microwave components, optical sensors, radiation detectors and computer switches [2,3].

There are many ways to produce thin films including sputtering, vacuum evaporation, laser ablation, chemical sol gel, etc.; the method used depends on the atomic composition and structure required and the intended application.

The physical properties of thin films are determined by their chemical composition, the concentration and the type of impurities, and the texture of the crystal or non-crystalline structure. Thus, ideally all these parameters should be known and, if possible, controlled during film

preparation. It is particularly important to produce a film with the required elemental composition, and it is therefore desirable to have a (non-destructive) method for measuring the composition. Some of these methods are electron and ion spectroscopy and x-ray fluorescence. Only an overview of the principles of these methods used for examining the chemical composition is given.

(1) Secondary ion mass spectrometry (SIMS); the film surface is bombarded by a beam of ions or atoms with energies in excess of 1keV. Atoms and cluster of atoms are knocked (sputtered) off the film surface and subjected to analysis in a standard mass spectrometer [2,4,5].

(2) Rutherford backscattering spectrometry (RBS); a beam of high energy (1MeV) ions produced by a nuclear particle accelerator is incident on the film. The energy and number of ions backscattered from the film may be analyzed to give the film composition [2,4,5,6].

(3) X-rays spectrometry; the intensity of the characteristic x-rays from the film may be analyzed to determine the chemical composition of the film. There are several different methods used to excite the characteristic x-rays; characteristic x-rays may be produced by bombarding the film with electrons (electron microprobe analysis, EMA), protons (proton induced x-ray emission, PIXE) or x-rays (x-ray fluorescence, XRF) [2,4,7].

SIMS is particularly sensitive for the measurement of film impurities but is a destructive analytical technique. RBS is a quantitative technique in its range of applicability, and is non-destructive if used properly; however it requires sophisticated equipment and is not available in most laboratories. XRF is a non-destructive technique and with suitable

calibration is quantitative. If microscopic resolution is required, then electron or proton microprobe characteristic x-ray analysis may be used.

Interest in the production of high-T_c supercoducting thin film at Brock University prompted us to consider methods for determining thin film composition. The principal objective of this thesis project was to assemble and calibrate an XRF system at Brock University for quantitative composition analysis of thin films.

This objective was accomplished in two steps. First the preparation of the thin film standards with known stoichiometry and second choosing an appropriate XRF set up for measuring the characteristic x-ray intensities reproducibly and accurately. Two different thin film standards were used: (a) chemical sol gel thin film with known stoichiometry, and (b) sputtered thin films with known stoichiometry as determined by RBS.

Excitation of the characteristic x-rays from the film was done by using a radioactive source (which produces line x-rays) instead of an x-ray tube (which produces continuous x-rays). The radioactive source excitation produced reliable, reproducible and accurate characteristic x-ray intensity measurements. Hence, a calibration constant ($C_{A,B}$) was obtained for some elements and the system was calibrated for Bi, Sr, Br, Cu, and Ca in the limit of thin films.

In recent years, a number of investigations of the use of XRF method to determine the composition of thin films have been reported in the literature. Some of these methods are ones that use standards for calibrating the observed intensity ratios of the elements in terms of known

atomic composition [8,9]. Some of these standards are filter standards [8] and solution standards [9]. In the case of filter standards, standard solutions with composition ratios according to the composition of the specimen are prepared. The standard solutions are transferred to a filter, the size of which is the same as the sample to be determined. The filters are then allowed to air dry, adhered to a blank substrate, and analyzed.

The disadvantages of these methods are that the thickness of the standards can not be measured. Other disadvantage is that continuous radiation is used which may produce diffraction peaks from the substrate or the film. These diffraction peaks can interfere with the measured fluorescent peaks and make the background subtraction difficult. Also by using a continuous radiation it is difficult to make a theoretical calculation of the composition.

In this project the type of the standards used is prepared originally on the substrate and the average thickness can be controlled and measured. Also the use of the x-ray line source with known energy made a theoretical calculation of the composition possible and background subtraction simple.

The outline of the thesis is as follows: Chapter (2) presents some theory appropriate to XRF, a theoretical calculation of the calibration constant and a theoretical model calculation of the absorption and secondary fluorescence effect. Chapter (3) describes the experimental apparatus of the XRF system. Chapter (4) describes methods of preparing thin film standards. Chapter (5) explains the difference of the x-ray spectra obtained both from the radioactive source and an x-ray tube. Also

shown are the details of the XRF x-ray spectra from the sources and the substrates and the analysis of the intensity measurements. In chapter (6) and (7) the experimental measurements of the calibration constant ($C_{A,B}$) for sol gel thin film standards and the sputtered films of known composition as determined by RBS are presented. Chapter (8) gives some of the applications of the XRF to the production of the high-T_c superconducting thin films produced at Brock University. Chapter (9) contains the conclusion.

(2) Theory

(2.1) Introduction:

In principle x-ray fluorescence analysis is a very simple technique. An x-ray beam strikes the sample to be analyzed in order to create inner-shell vacancies in the sample atoms; a detector records the corresponding characteristic x-rays produced. The intensity of the characteristic x-rays is a measure of the number of corresponding sample atoms. A brief summary of these fundamentals will be given.

(2.2) Characteristic X-rays:

Figure 2.1 shows the binding energies of electrons in the subshells of an atom and the corresponding quantum numbers (n **l** j) [10]. A characteristic x-ray photon (energy $E_{C,P}$) may be emitted when an electron undergoes a transition to a vacant state in subshell with larger binding energy. This photon energy is given by $E_{C,P} = B_f - B_i$, where B_i and B_f are the binding energies of the electron in its initial and final state respectively.

Table 2.1 gives the conventional notation for the principal (large intensity) K and L x-rays. The principal x-rays obey the quantum number selection rule;

$$\Delta \mathbf{l} = \pm 1 \quad , \quad \Delta j = 0 , \pm 1$$

i.e., transitions take place only between levels whose **l** quantum numbers differ by one and whose j quantum number differ by zero or one [10]. The

relative intensities of the different K x-rays and L x-rays have been measured and are tabulated in the literature [11].

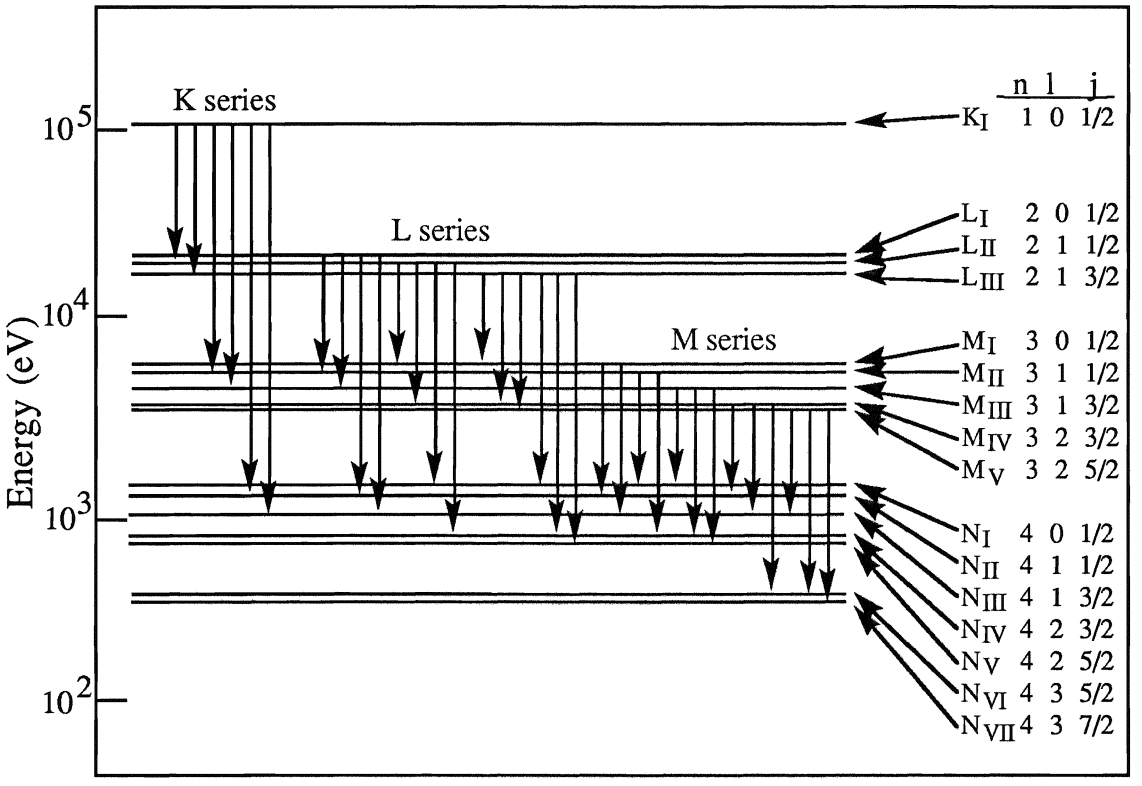

Fig. 2.1 A diagram of a higher energy x-ray levels for the uranium atom and the transitions between these levels allowed by the selection rules.

Table 2.1

$K\alpha_1 = K - L_{III}$	$L\alpha_1 = L_{III} - M_V$
$K\alpha_2 = K - L_{II}$	$L\alpha_2 = L_{III} - M_{IV}$
$K\beta_1 = K - M_{III}$	$L\beta_1 = L_{II} - M_{IV}$

(2.3) Fluorescence yield:

Not all electron vacancies will result in the production of characteristic x-rays. A significant proportion of the electron transitions to the initial vacancy result in the emission of an Auger electron rather than

an x-ray photon [7,12]. Figure 2.2 gives an example of the emission of an Auger electron.

For vacancies in the K shell (for example), the Auger process is initiated when an outer electron such as an L_1 electron fills the hole. The energy released can be given to another electron such as an L_1 electron which is then ejected from an atom. In this case the energy of the outgoing electron is $K_e = B_K - 2B_L$ as indicated in figure 2.2.

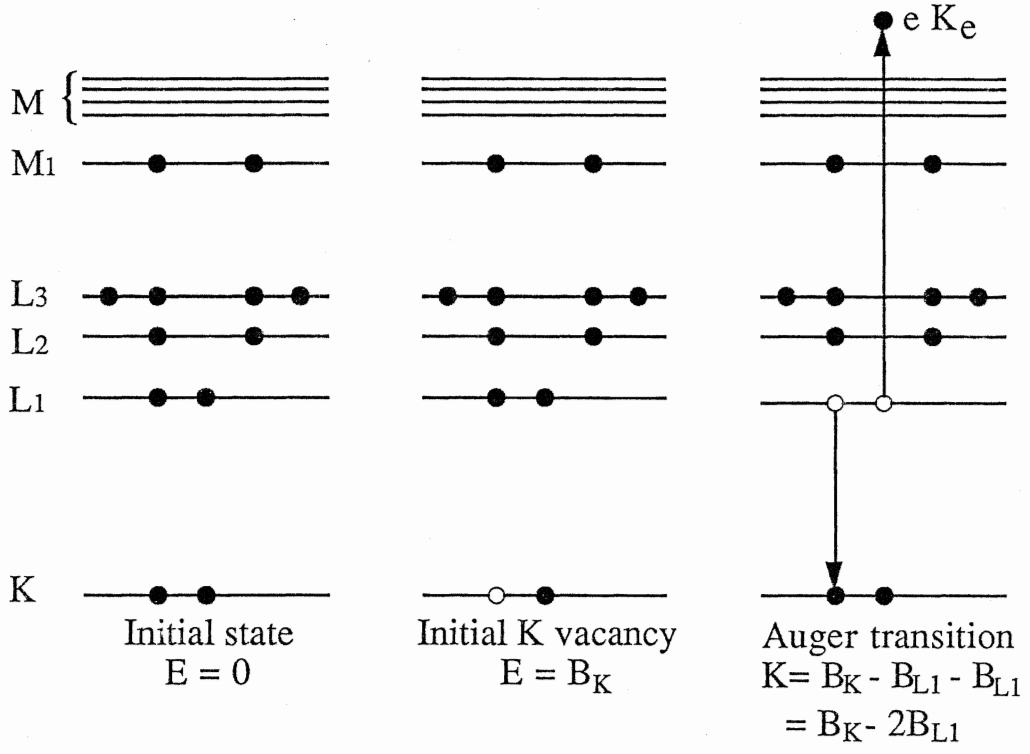

Fig. 2.2 Auger transition corresponding to an initial K hole which is filled with an L_1 electron and simultaneously the other L_1 electron is ejected.

The probability of the Auger process can be found from the fluorescence yield (ω). For example, the fluorescence yield for the K shell vacancy, ω_K is the average number of the K x-ray photons produced

per K shell vacancy, and similarly for the L shell vacancy. It is a function of both the atomic number and the location of the initial vacancy [4,12,13].

(2.4) Photoelectric absorption:

Two different radiations can be used to create inner-shell vacancies: (1) photon radiation (x-rays), or (2) charged particle radiation (electrons, protons, alpha particles, etc.).

In the x-ray fluorescence, photon excitation is used. The photons can interact with the atoms in the sample by four different processes: photoelectric, pair production, Rayleigh (elastic scattering) and Compton (inelastic scattering). The first two absorb photons completely, while the last two only scatter them.

The probability that a photon will interact with an atom is expressed in terms of the total cross section (σ_T), which is the sum of the scattering (σ_S), photoelectric (σ_{PE}), and pair production (σ_{PR}) cross sections. The elastic and inelastic scattering cross sections are small if the photon energy is smaller than 100keV, which is the case in our experiment, and the minimum photon energy needed to create an electron positron pair is 1.022MeV. Therefore, the interaction between the x-ray photons and the atoms in the sample, in our case, is dominated by photoelectric absorption.

In the photoelectric absorption of a photon, the photon energy, E_P, is completely converted and transferred to an electron which is ejected from the atom with kinetic energy $K_e = E_P - B$, where B is the binding energy of the electron. This process requires a minimum energy equal to the binding energy, B, of the electron.

The probability that a photon will undergo photoelectric absorption is expressed in terms of the photoelectric cross section, σ_{PE}, which is defined as

$$\sigma_{PE} = \frac{N}{Int} \tag{2.1}$$

where N is the number of photons absorbed in a thin sample, thickness t(cm) and atomic density n(atoms/cm^3) when bombarded by I excitor photons incident normally on the sample surface; σ_{PE} has the units of cm^2/atom.

Figure 2.3 shows the photoelectric cross section, σ_{PE}, as a function of the photon energy for the strontium atom. The photoelectric cross section exhibits sharp discontinuities called absorption edges which occur at the binding energies for the different electrons in the strontium atom. The photoelectric absorption is energetically possible for $E_P > B$ but is forbidden for $E_P < B$; consequently there is a discontinuous decrease in σ_{PE} as E_P is decreased through an absorption edge [7,10,12].

σ_{PE} increases with decreasing E_P and increasing atomic number (Z). For example, the predicted cross section per atom for photoelectric absorption on a K shell electron is [15]

$$\sigma_{PE} = \frac{8\pi}{3} (e^2/mc^2)^2 \, 4\sqrt{2} \left(\frac{1}{137}\right)^4 Z^5 \left(\frac{mc^2}{E_P}\right)^{\frac{7}{2}} \tag{2.2}$$

The very strong Z dependence of σ_{PE} reflects the fact that a K shell electron becomes much more tightly coupled to the nucleus with increasing Z.

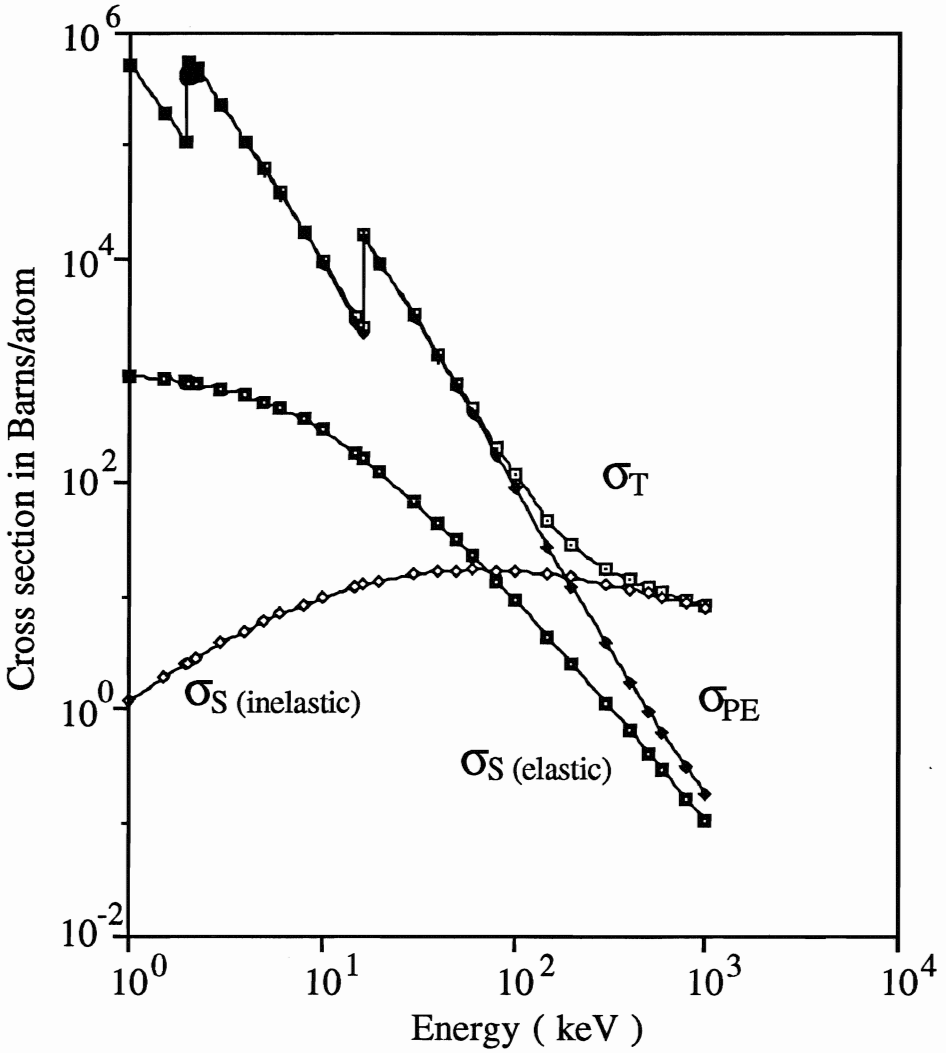

Fig. 2.3 The scattering, photoelectric, and total cross sections for the Sr atom [14].

(2.5) Absorption of Mo K radiation in $Bi_2Sr_2Ca_1Cu_2O_X$ film:

As an example in the present work, consider the photoelectric absorption of Mo Kα x-ray used as excitor photons (E_P = 17.441 keV) incident on

a superconducting oxide film $Bi_2Sr_2Ca_1Cu_2O_8$. The fraction of the incident photons absorbed is

$$\frac{Io - I}{Io} = 1 - e^{-\mu_m \rho t} \qquad (2.3)$$

where ρ is the density of absorber (g / cm^3).

t is the thickness of the film (cm).

μ_m is the mass absorption coefficient (cm^2/g)

For a multielement film

$$\mu_m = \sum_i W_i \mu_{mi}$$

where W_i is the weight fraction of element i in the oxide and μ_{mi} is its mass absorption coefficient.

Table (2.2) list the fraction of Mo Kα x-rays absorbed in the oxide for different thickness.

Table 2.2

Film	* ρ	μ_m	Fraction absorbed		
	g/cm^3	(cm^2/g)	1 kÅ	5 kÅ	10 kÅ
$Bi_2Sr_2Ca_1Cu_2O_8$	6.5	91.474	0.006	0.029	0.058

* The value of ρ was taken from reference [16].

(2.6) X-ray fluorescence cross section:

The Kα x-ray fluorescence cross section, $\sigma_{K\alpha}$, is a measure of the probability that an atom will absorb an excitor photon and produce a Kα x-ray. $\sigma_{K\alpha}$, is related to the photoelectric cross section σ_{PE} by [17]

$$\sigma_{K\alpha} = \sigma_{PE} \left(1 - \frac{1}{J_K}\right) \omega_K f_{K\alpha} \qquad (2.4)$$

Where J_K is the K shell jump ratio and $\left(1 - \frac{1}{J_K}\right)$ is the fraction of the photoelectric absorptions which produce a K shell vacancy.

ω_K is the K fluorescence yield.

$f_{K\alpha}$ is the fractional x-ray emission rate (the fraction of Kα emission over the total K emission).

A similar equation is used for the L x-ray lines.

C. Bhan et al.[17] have reported very good agreement between the measured and calculated x-ray fluorescence cross section for certain elements, but regrettably not for the elements we have to measure.

(2.7) Measurements of the stoichiometry of films:

Using the XRF technique the stoichiometry of a sample is determined from the number of counts in the fluorescent x-ray peaks of the spectrum (the x-ray yield).

(I) Thin samples: For thin samples, where photon absorption is negligible, the x-ray yield of each peak is [13,18]

$$Y = n\,\sigma\,I_o\,t\,\varepsilon\,\frac{d\Omega}{4\pi} \qquad (2.2)$$

where n is the number of atoms per unit volume (atoms/cm^3).

σ is the x-ray fluorescence cross section of an element for a given characteristic x-ray line (cm^2/atom).

I_o is the photon intensity, that is the number of photons striking the sample per second.

ε is the detector efficiency for the characteristic x-rays from an element.

t is the thickness of the sample (cm).

$d\Omega$ is the solid angle subtended by the detector (steradian).

One is generally interested in measuring the relative concentrations, $\frac{n_A}{n_B}$, of elements A and B in a sample, so that only the ratio of the x-ray yields, $\frac{Y_A}{Y_B}$, is required. The stoichiometry ratio is then

$$\frac{n_A}{n_B} = \frac{Y_A}{Y_B}\,\frac{\sigma_B\,I_{oB}\,\varepsilon_B\,d\Omega_B}{\sigma_A\,I_{oA}\,\varepsilon_A\,d\Omega_A} \qquad (2.3)$$

If the detector efficiency for x-rays from element A and B is 100% (i.e. $\varepsilon_A = \varepsilon_B$) and element A and B are fluoresced simultaneously by the same source then I_o and $d\Omega$ are the same for the two elements in the sample, then the stoichiometry ratio can be written as

$$\frac{n_A}{n_B} = C_{A,B}\,\frac{Y_A}{Y_B} \qquad (2.4)$$

Where $C_{A,B} = \frac{\sigma_B}{\sigma_A}$

Equation 2.4 has a linear relationship between the atomic ratio $\frac{n_A}{n_B}$ and the intensity ratio $\frac{Y_A}{Y_B}$, where the proportionality constant is $\frac{\sigma_B}{\sigma_A}$. The constant $C_{A,B}$ can be determined by two ways: (a) theoretically using the fluorescence cross section, σ, and (b) experimentally using a representative set of thin film standards of known stoichiometry.

(a) Theoretical calculation of $C_{A,B}$: For a given exciting energy and a given x-ray line (say $K\alpha$) the constant $C_{A,B}$ is determined as

$$C_{A,B} = \frac{\sigma_B}{\sigma_A} = \frac{\sigma_{PB}\,(1 - \frac{1}{J_{KB}})\,\omega_{KB}\,f_{K\alpha B}}{\sigma_{PA}\,(1 - \frac{1}{J_{KA}})\,\omega_{KA}\,f_{K\alpha A}}$$

where the values of σ_P and J_K, ω_K ,and f_K were taken from references [14], [11], and [19] respectively.

This constant has been calculated theoretically for $C_{Cu,Z}$ ($25<Z<39$) using Mo K excitor radiation. The values of the theoretical results are shown in table 2.3 and plotted versus Z in figure 2.4.

Table 2.3

Z	26	28	29	30	32	34	35	36	38
$C_{Cu,Z}$	0.524	0.819	1	1.23	1.66	2.24	2.56	2.95	3.63

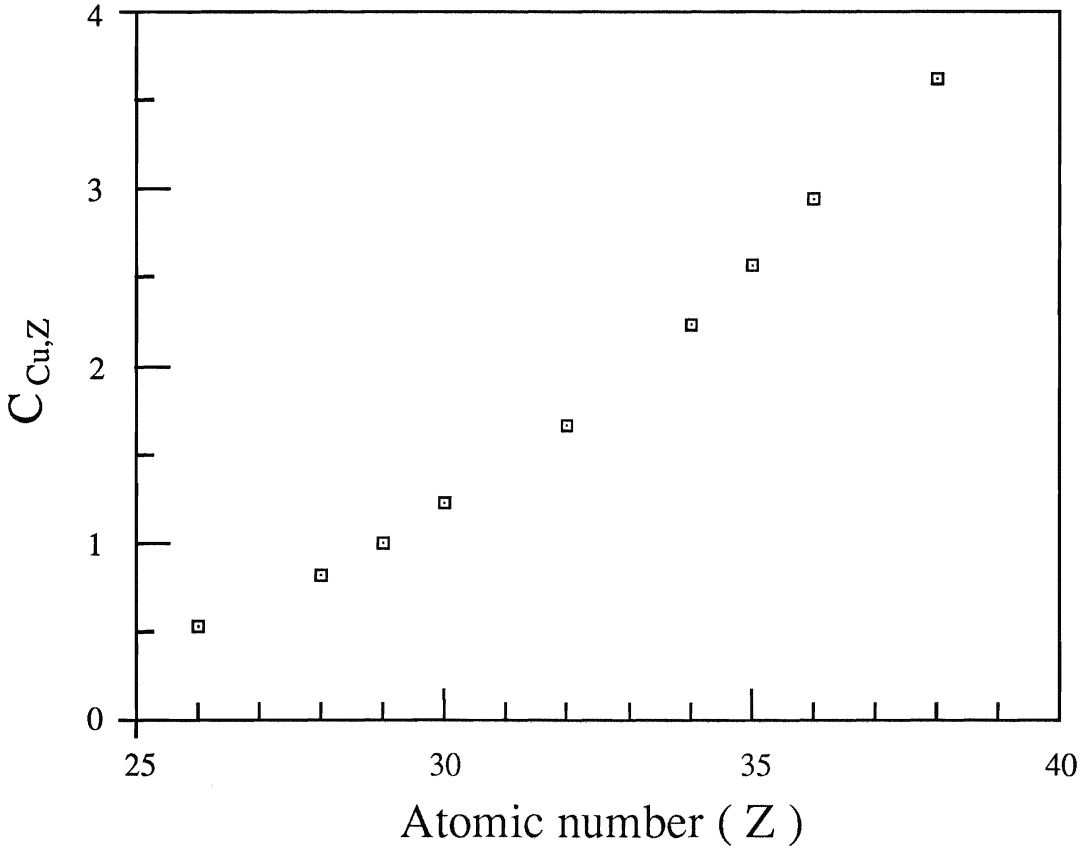

Fig. 2.4 A graph of a theoretical calibration constant of $C_{Cu,Z}$ versus Z.

(b) Experimental determination of $C_{A,B}$: The constant $C_{A,B}$ was determined experimentally by measuring the intensity ratio $\frac{Y_A}{Y_B}$ from thin films of known stoichiometry $\frac{n_A}{n_B}$ as in equation 2.5. This represents an experimental calibration of the XRF system.

$$C_{A,B} = \frac{n_A/n_B}{Y_A/Y_B} \tag{2.5}$$

Two different sets of thin film standards were used for generating a reliable calibration of the XRF system. The first set of standards was a set of sol gel films with known chemical composition and second set of standards was a set of sputtered films of known $\frac{n_A}{n_B}$ as determined from RBS.

(II) Thick samples: In thick films, absorption and secondary fluorescence may be come significant. Secondary fluorescence is expected when the incident radiation has a high photon energy, and there is an atom A that absorbs the incident radiation very strongly and produces a characteristic x-ray that fluoresces atom B. The measured x-ray yield ,Y, can be written in terms of primary ,Y_P, and secondary ,Y_S, fluorescence as

$$Y = Y_P + Y_S$$

$$Y = Y_P \left(1 + \frac{Y_S}{Y_P} \right)$$

$$Y = Y_P (1 + S) \tag{2.6}$$

where S is the secondary fluorescence factor.

If absorption is taken into account, the primary x-ray yield ,Y_P, is expressed as [18]

$$Y_P = n \sigma I_o \varepsilon \frac{d\Omega}{4\pi} a \tag{2.7}$$

where a is the absorption factor given by

$$a = \frac{1}{(\mu m + \mu m')\,\rho}\left[\,1 - e^{-(\mu m + \mu m')\rho t}\,\right]$$

μm and $\mu m'$ are the mass absorption coefficients of the sample for the incident radiation and for the characteristic radiation of an element respectively.

ρ is the mass density of the sample.

Equation (2.7) assumes, for simplicity, normal incidence of the exciting photons and backward x-ray detection; this is a reasonable approximation to the XRF system geometry used. Then the relative concentration, $\frac{n_A}{n_B}$, of elements A and B in a sample can be written as

$$\frac{n_A}{n_B} = \frac{Y_A}{Y_B}\,\frac{\sigma_B}{\sigma_A}\,\frac{(1 + S_B)}{(1 + S_A)}\,\frac{a_B}{a_A} \qquad (2.8)$$

Equation (2.8) assumes that the detector efficiency from elements A and B is 100% and that elements A and B are fluoresced simultaneously with the same source (i.e. I_o,t ,and $\frac{d\Omega}{4\pi}$ are the same).

(2.8) Absorption and secondary effect:

The secondary fluorescence factor, S, can be estimated approximately using the following model:

The model assumes that all primary x-rays from A (N_{PA}) are produced at the center of the film and are emitted in all directions,θ ,with equal probability. Figure 2.5 shows a schematic diagram of the model,

where d and t are the diameter and the thickness of the film respectively. In this project $t \leq 5000\text{Å}$ and $d \sim 0.8\text{cm}$ (i.e. $\frac{t}{d} \sim 6\text{x}10^{-5}$)

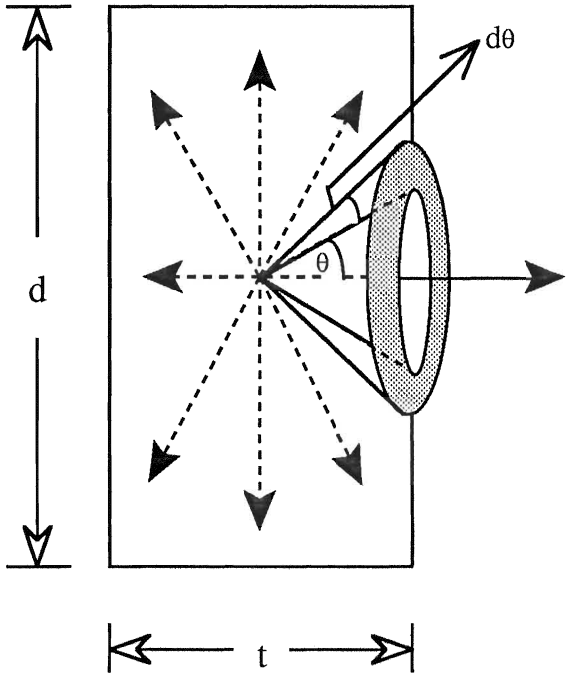

Fig. 2.5 Schematic diagram of a model used to calculate the secondary fluorescence.

The secondary fluorescence from B which is produced by absorption of the primary x-rays which leave the center of the film in the range of θ and dθ is

$$\Delta N_{SB,A} = \frac{1}{2} N_{PA} \frac{2\pi \sin\theta}{2\pi} d\theta \left[1 - \exp-(\mu_A \frac{t/2}{\cos\theta}) \right] \frac{n_B \sigma_{BA}}{\mu_A}$$

where $\frac{1}{2} N_{PA} \frac{2\pi \sin\theta}{2\pi} d\theta$ is the number of the primary x-rays from A produced in the direction of θ.

$\left[1 - \exp-(\mu_A \frac{t/2}{\cos\theta})\right]$ is the fraction of primary x-rays absorbed along their way out to the film surface.

$\frac{n_B \sigma_{BA}}{\mu_A}$ is the fraction of primary x-rays which are absorbed that produce characteristic radiations from B.

μ_A is the linear absorption coefficient for the primary x-rays from A in the film.

σ_{BA} is the x-ray fluorescence cross section of element B from x-rays from element A.

The total secondary fluorescence from B produced by absorption of primary x-rays of A is

$$N_{SB,A} = 2 \int_{\theta=0}^{\pi/2} \Delta N_{SB,A}$$

$$N_{SB,A} = N_{PA} \frac{n_B \sigma_{BA}}{\mu_A} \int_{\theta=0}^{\pi/2} [\, 1 - \exp-(\mu_A \frac{t/2}{\cos\theta})] \sin\theta \, d\theta$$

In order to calculate approximately the above integral the function

$$y = [\, 1 - \exp-(\mu_A \frac{t/2}{\cos\theta})]$$

was approximated by $y = \mu_A \frac{t/2}{\cos\theta}$ for $0 < \theta < \theta'$

and $y = 1$ for $\theta' < \theta < \pi/2$

and when $\theta = \theta'$ $\mu_A \frac{t/2}{\cos\theta} = 1$

This approximation of the integral is an over estimate of $N_{SB,A}$. Then the integral can be written as

$$N_{SB,A} \approx N_{PA} \frac{n_B \sigma_{BA}}{\mu_A} \{ \int_0^{\theta'} \mu_A \frac{t/2}{\cos\theta} \sin\theta \, d\theta + \int_{\theta'}^{\pi/2} \sin\theta \, d\theta \}$$

$$N_{SB,A} \approx N_{PA} \frac{n_B \sigma_{BA}}{\mu_A} [\mu_A \frac{t}{2} \{ - \ln(\cos\theta') \} + \cos\theta']$$

where $\cos\theta' = \mu_A \frac{t}{2}$

Hence $N_{SB,A} \approx N_{PA} n_B \sigma_{BA} \frac{t}{2} \{1 - \ln(\mu_A \frac{t}{2})\}$

Also $N_{PA} \approx I_o n_A \sigma_A t$

$N_{PB} \approx I_o n_B \sigma_B t$

Now the secondary fluorescence factor of B from A is

$$S_{B,A} = \frac{N_{SB,A}}{N_{PB}} \approx \frac{n_A \sigma_A \sigma_{BA}}{\sigma_B} \frac{t}{2} \{1 - \ln(\mu_A \frac{t}{2})\}$$

If B has secondary fluorescence contributions from several different elements j, then the sum of all secondary fluorescence factors is taken.

$$S_B = \sum_j S_{B,j}$$

The contribution of absorption and secondary fluorescence of equation (2.8) was calculated for Cu and Bi present in $Bi_2Sr_2Ca_1Cu_2O_8$ thin film (5000Å). In this film, for example, Cu has secondary fluorescence

contributions from two atoms (Bi and Sr), and Bi has secondary fluorescence contributions to its L lines from Sr. Hence equation (2.8) has a correction factor $[\frac{(1 + S_B)}{(1 + S_A)} \frac{a_B}{a_A}]$ of 0.95 for $\frac{n_{Cu}}{n_{Sr}}$ and 0.96 for $\frac{n_{Cu}}{n_{Bi}}$. These corrections are small and comparable to the accuracy of the XRF measurements and therefore are not significant in most cases considered in this work. For an ideal thin film, these corrections are equal to one.

(3) Apparatus

The x-ray system used in this project consisted of an x-ray source, thin film sample, and an x-ray photon energy spectrometer including detector, pulse amplifier, and multichannel analyzer (MCA). Figure 3.1 shows a block diagram of the system.

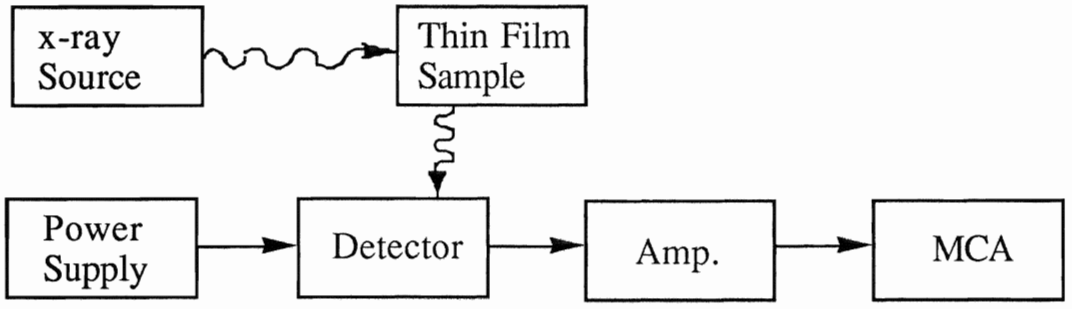

Fig. 3.1 Block diagram of the apparatus.

(3.1) X-ray Source:

Two sources of x-ray radiation were available for use in this experiment; (i) an x-ray tube (continuous radiation), and (ii) a radioactive source (monoenergetic radiation). One source may hold an advantage over the other depending on the analytical problem involved.

(i) X-ray Tube:

Electrons are accelerated from a filament (cathode) across a potential difference of a maximum 60 kV to a metal anode (in our case molybdenum). X-rays are produced in collisions between the electrons and the anode atoms. Most of the electron energy is converted into heat and not to x-rays, and therefore it is essential to water-cool the anode target to prevent its melting [12].

(ii) radioactive Sources:

Two different radioactive sources were used in this project, 100mCi ^{241}Am and 10mCi ^{55}Fe sources. The ^{241}Am source emits γ-rays of energy 59.5 keV and the ^{55}Fe source emits photons of energy 5.894 keV.

In order to get the best efficiency in exciting the sample atoms, the excitation energy of the source should be just above the absorption edge of the element in the sample. For this reason several radioactive sources with a variety of monoenergetic photons are needed in order to excite a wide range of elements in the sample. For this reason, a secondary source excitation can be used. In this process, the monoenergetic photons from the radioactive source are used to excite a target of known element. This will result in the production of x-rays characteristic of the atoms in the target. These target x-rays are in turn used to fluoresce the elements in the sample to be analyzed.

For example, the ^{241}Am radioactive source was used to produce a secondary photon of energy 17.441 keV from a Mo secondary target. This secondary photon can be used efficiently to fluoresce characteristic K x-rays from elements with $20 \leq Z \leq 39$. On the other hand ^{55}Fe source was used to fluoresce elements with $17 \leq Z \leq 20$. Figure 3.2 shows a schematic diagram of a radioactive source with and without secondary targets.

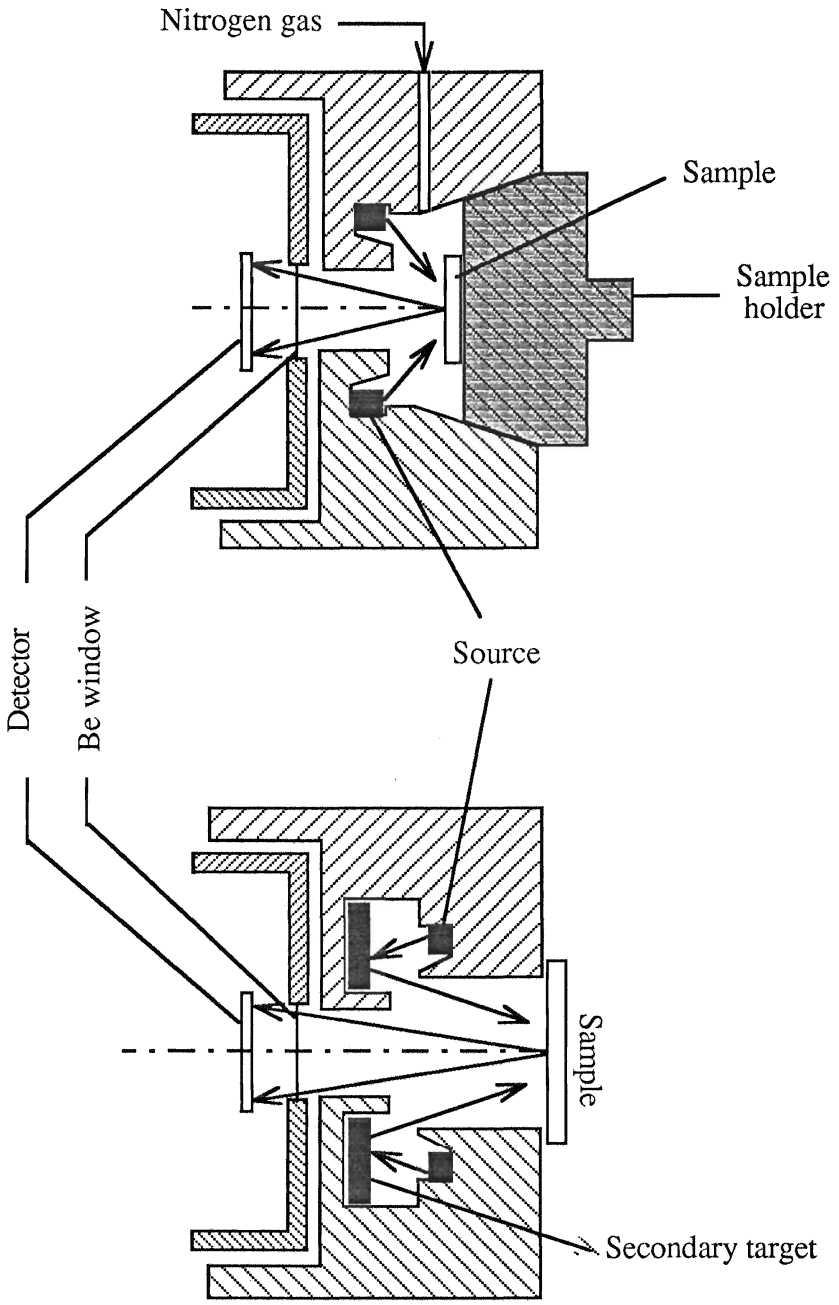

Fig. 3.2 Schematic diagram of a radioactive source with and without secondary targets.

(3.2) Detector:

The detector used in this project was an EG & G ORTEC Si(Li) x-ray detector which converts an x-ray photon into an electric pulse [20]. The

amplitude of this electric pulse is proportional to the energy deposited by the photon in the detector. It is operated at the temperature of liquid nitrogen (77^{o} K) and at a bias of -1200 Volts. The electric charge pulses produced by the detector are transferred to the pulse amplifier then to the multichannel analyzer (MCA).

(i) Detector energy resolution:

The amplitude of pulses due to x-ray photons of energy E are distributed around a particular value Ep as shown in figure 3.3, where Ep is equivalent to E.

In figure 3.3 the counting rate is equivalent to the number of pulses having a particular amplitude. If the width of the curve at half its maximum height is ΔE and if Ep is the mean pulse amplitude, then the energy resolution, R, of the detector is $R = \frac{\Delta E}{Ep}$. The smaller R (or the smaller ΔE) the better the resolution [12,21].

Usually ΔE is measured from a standard reference Mn Kα line of energy 5.894keV (Ep). The ΔE in our case is 0.178keV; therefore, the resolution $R = \frac{\Delta E}{Ep}$ of the Si (Li) detector is 3.0% at 5.894keV.

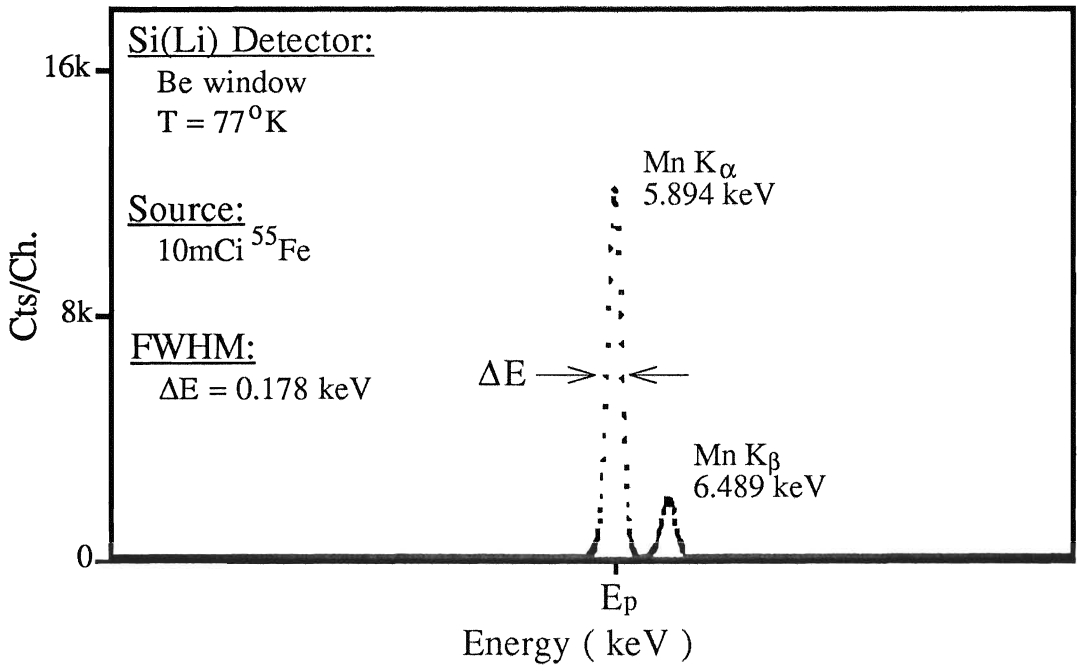

Fig. 3.3 Detector resolution spectrum

(ii) Detector Efficiency:

The efficiency is the number of x-ray quanta absorbed by the detector (N_a) per the number of x-ray quanta incident on the detector (N_i), i.e. $\frac{N_a}{N_i}$ x 100%.

The detector used has a thin beryllium (Be) window through which the x-ray energy photons must pass before reaching the active part of the detector (Si(Li) part). Note that the photon absorption by the detector depends on the energy.

Figure 3.4 shows that:

(a) for x-ray energy photons with energy about 3 - 25 keV, the efficiency is about 80 - 100%

(b) for x-ray energy photons with energy less than 3 keV, the efficiency decreases to zero due to the Be window absorption of low energy photons.

(c) for x-ray energy photons with energy greater than 25 keV, the efficiency tends to zero due the very high energy photons passing through the Be window and Si(Li) detector without getting absorbed.

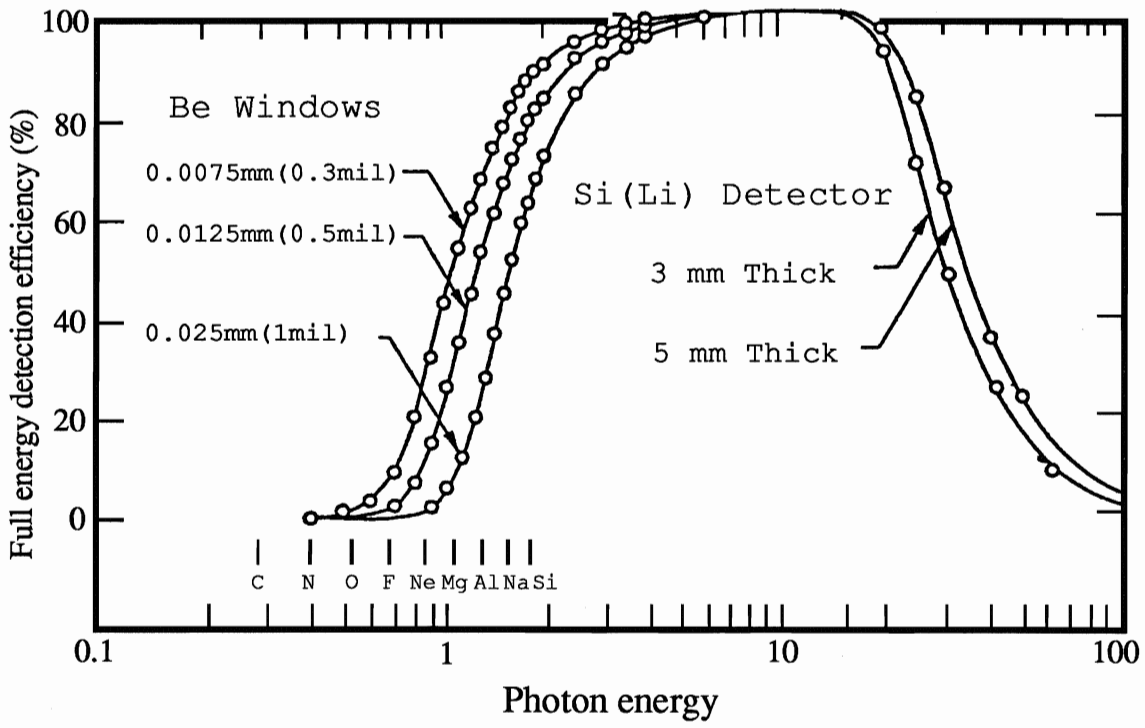

Fig. 3.4 Detection efficiency diagram [20].

(3.3) Multichannel Analyzer (MCA):

It is designed to sort pulses from the detector into channels according to their energy. A Packard Bell computer was used to display

the energy distribution as the number of counts in each channel vs. the channel number; this distribution is called the MCA spectrum.

If the x-ray energy photons that have to be examined range from 0 - 20keV and the MCA has 1000 channels, then the spectrometer amplifier gain is set so that each channel spans an energy of 20eV.

(4) Thin Film Preparation

(4.1) Introduction:

Since the discovery of the Bi-Sr-Ca-Cu-O superconductor, several techniques have been employed to prepare these thin films. They include techniques such as magnetron sputtering [22], vacuum evaporation [23], laser ablation [24], and chemical sol gel techniques [25].

(4.2) Sputtering Method:

The sputtering system used to prepare thin films was assembled at Brock university. It has a US GUN II R. F. Planar Magnetron sputtering source with three independent water cooled targets of 25mm in diameter and 3mm thick. The sputtering source may be operated either using an R.F. or a D.C. power supply and the system was pumped with a high vacuum pump of a cryo type. Figure (4.1) shows a schematic diagram of the sputtering system. Thin films of Bi-Sr-Ca-Cu-O, Bi-Ca-Cu-O, and Sr-Ca-Cu-O were prepared from different targets:

(i) Sintered Targets : These targets were prepared using the desired stoichiometric amount of Bi_2O_3, $SrCO_3$, $CaCO_3$, and CuO powders. These amounts were mixed together and ground for 1hr. to a very fine powder in a mortar with two pestles. The fine powder was then heated at ~840^o c for 24 hr. and was left inside the oven to cool down. The heated sample was then ground again, pressed into tablets of a diameter of 25mm, and heated again for 3 days at 816^{o}c.

(ii) Melt Cast Targets: These targets were obtained by mixing the desired stoichiometric amount, then casting the melt in a copper mold of a diameter of 25mm. Subsequently, annealing at 750^{o}c was done to improve the thermal conductivity of these targets. The simplicity of making these targets allowed us to easily change the composition of the targets to obtain films of a different composition. These targets were found to be denser than the sintered target and to take more power.

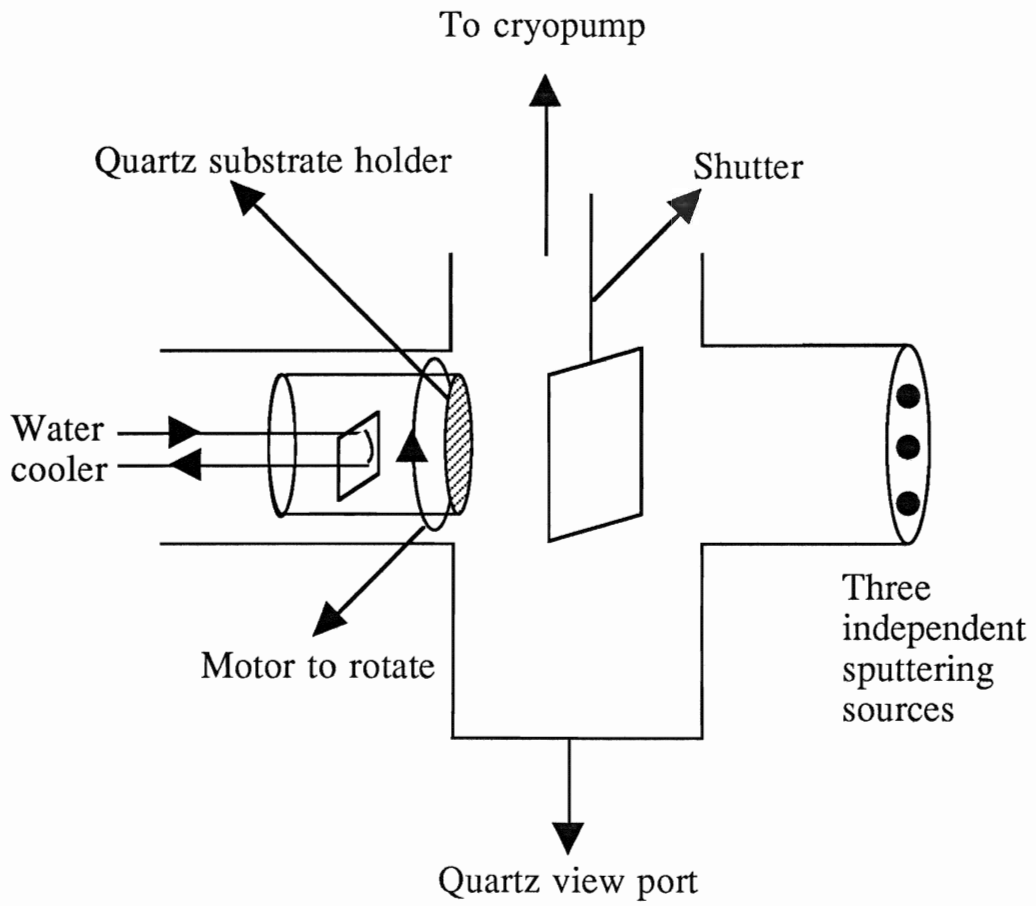

Fig. 4.1 A schematic diagram of the sputtering system

The targets were sputtered onto single crystal MgO substrates. The sputtering process was generally carried out at different pressures, power, and time to obtain different thicknesses of thin films. The thicknesses of the thin films were measured approximately by using an optical interferometer.

(4.3) Chemical Sol Gel Method:

The term sol gel is derived from the definition of sol and gel. A sol is a suspension of solid particles in a liquid. A gel on the other hand is defined as a two-component system of a semisolid nature, rich in liquid [26].

The basic idea of this method is to prepare a metalorganic solution of the required chemical composition and then to form a thin film of this solution on the substrate. Finally, the thin film solution is dried to form a sol gel film of known stoichiometry.

The preparation techniques used were developed from those described by Hussain and Sayer [25] and by V. Slusarenko et al. [27]. Unfortunately their prescription is not always successful for the chemical compositions we required. It was found that the addition of EDTA (Ethylenediaminetetra-acetic acid disodium salt) assisted in the formation of a solution of the required chemical composition.

A stoichiometric mixture of the required metal nitrates was dissolved in distilled water in the desired proportion and mixed with EDTA, acetic acid, and ethylene glycol. The molar ratio of EDTA to the total metal nitrate was fixed at two, which appears to be the minimum ratio

needed to dissolve all the nitrates. The ethylene glycol was used partly as a solvent, but also to make the solution viscous and homogeneous. Consequently, the concentration and the viscosity of the solution can be adjusted as required. The prepared solution was heated for several hours at low temperature with stirring sometimes to completely dissolve the metal nitrates.

A variety of thin films of different chemical compositions and thickness were produced on quartz substrates using the prepared solution. The thin films were formed by either dip coating the substrate into the solution or by placing small drops on the substrate. After the coating, the films were dried either in air or by firing the film on a hot plate. The coating and drying were repeated if necessary until a desired film thickness was achieved. The thicknesses of the films were measured by using an optical interferometer. The films were not always of uniform thickness; the average thickness of the films varied from 0.1μm to 3μm.

(5) X-ray spectra

(5.1) Choice of x-ray source:

Initially the analysis of thin films was performed using x-rays from a Mo x-ray tube. Because the beam was collimated (1mm), this technique had the advantage that it could be used to sample various regions of the film and hence, check for homogeneity. Also all the atoms of the film can be fluoresced simultaneously. However, the disadvantages greatly outweighed the advantages. It was found that the continuous radiation from the x-ray tube was diffracted from the underlying single crystal substrate and produced structure in the spectra which made background subtraction and fluorescent peak intensity determination less certain. Also the realignment of the film to reproduce the XRF beam-sample-detector arrangement was difficult.

To avoid some of these difficulties it was decided to use a radioactive x-ray source. This had the advantage of eliminating diffraction from the substrate and providing a much smoother background in the spectra. However the ability to sample various regions of the film was lost due to the fact that the entire film was illuminated simultaneously. Figures 5.1 and 5.2 show spectra of BiSrCaCuO film on MgO substrate fluoresced by using both the x-ray tube and the radioactive source. It can be seen from these figures how the diffraction peaks interfered with the fluorescent peaks in figure 5.1, whereas in figure 5.2 the fluorescent peaks are superimposed on a smooth background.

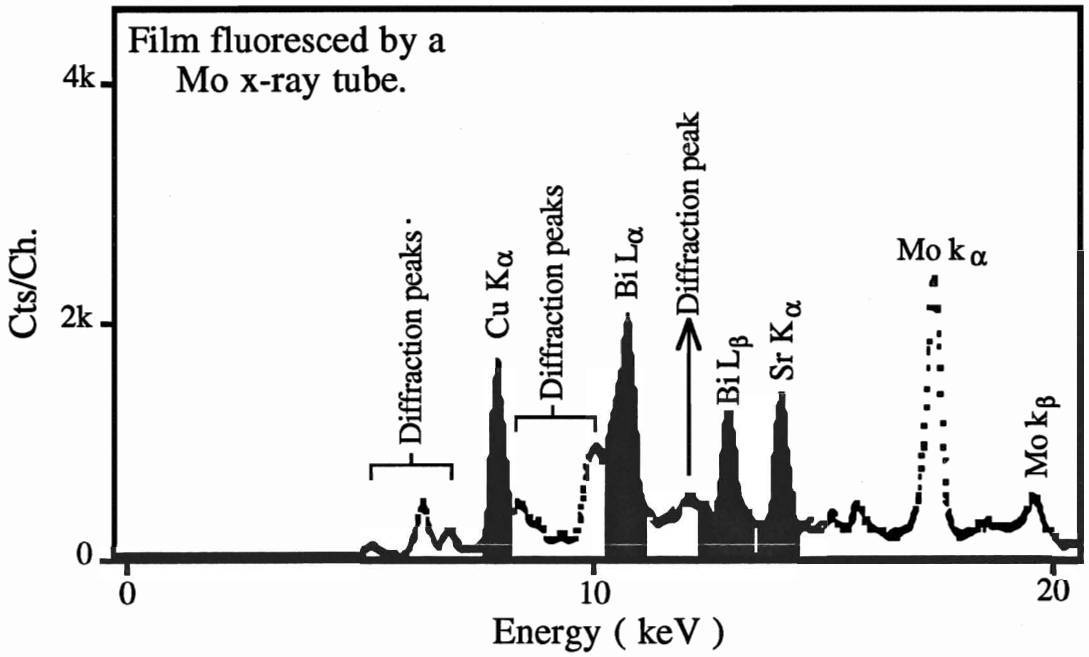

Fig. 5.1 X-ray spectrum from Bi-Sr-Ca-Cu-O film on MgO substrate.

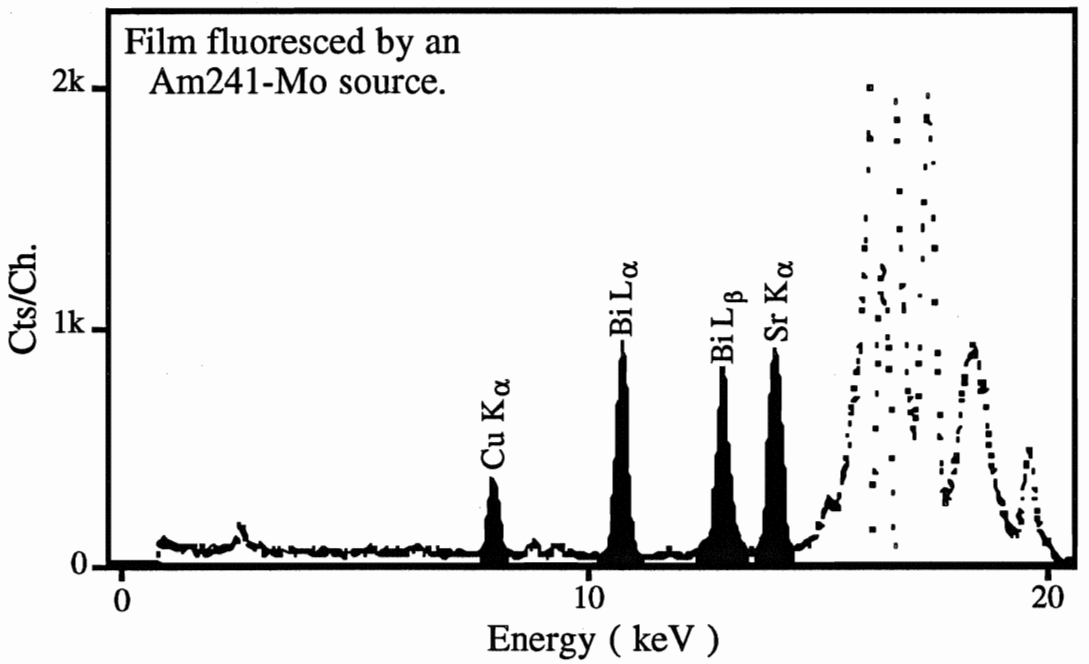

Fig. 5.2 X-ray spectrum from Bi-Sr-Ca-Cu-O film on MgO substrate.

The XRF calculation method of the thin film analysis requires the precise knowledge of the energies of the excitor. The radioactive source made the calculation of the thin film stoichiometry from the measured fluorescent yield ratios simple. Also it was necessary to know the full energy peaks spectrum of the excitor to ensure that there are no extra energy peaks in addition to the major emission peaks. The choice of the radioactive source and the secondary target to fluoresce elements present in the film is determined by considering factors such as optimum excitation efficiency and peak interference. Sometimes, the sample contains more than one element and in order to efficiently excite all of them, two or more excitor sources are used.

(5.2) Radioactive source spectra:

In this work two radioactive sources were used, Am241-Mo and ^{55}Fe sources. The Am241-Mo source was used to produce fluorescent K x-rays of Cu, Br, Sr, and L x-rays of Bi, and the ^{55}Fe source to produce fluorescent K x-rays of Ca. Figure 5.3 shows an energy spectrum of Am241-Mo source. It consists of two lines MoKα and MoKβ. These lines have specific energies of 17.441 keV and 19.605 keV respectively. Figure 5.4 shows on the other hand an energy spectrum of the ^{55}Fe source which consists of two lines Mn Kα (5.894 keV) and Mn Kβ (6.489 keV).

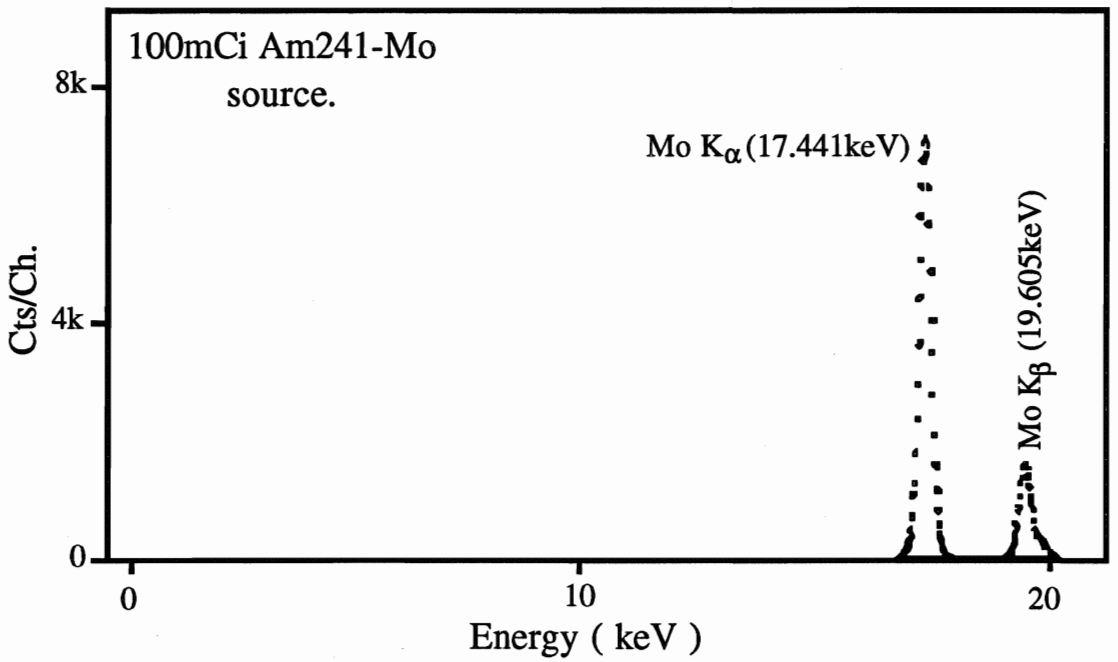

Fig. 5.3 X-ray line spectrum from a radioactive source.

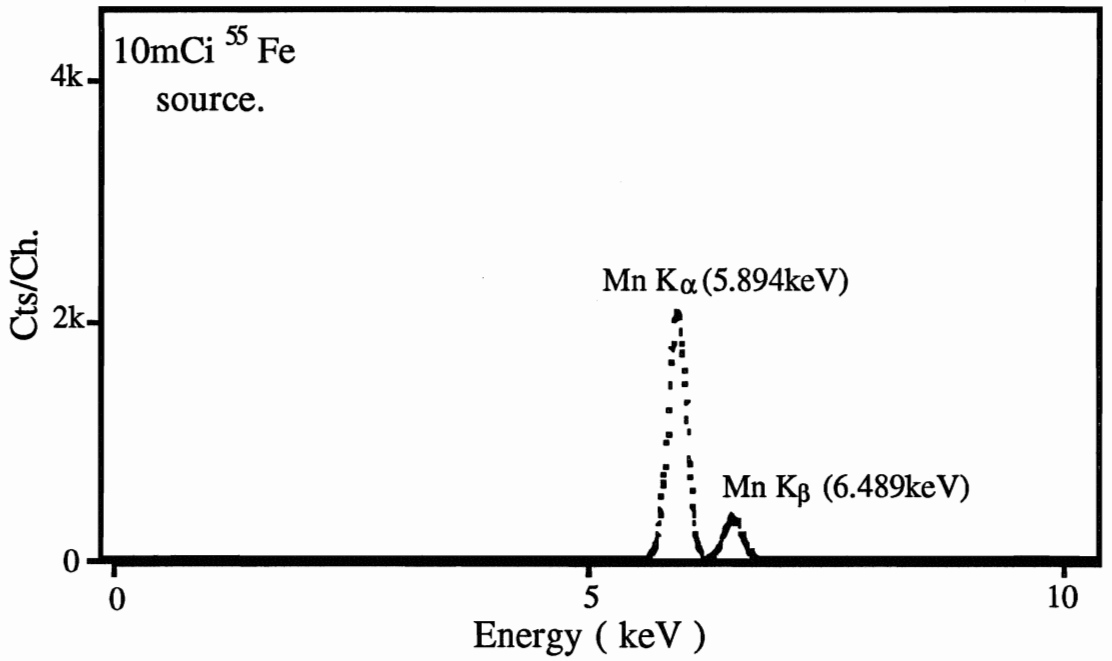

Fig. 5.4 X-ray line spectrum from a radioactive source.

(5.3) MgO and Quartz substrate spectra:

(i) Am241-Mo Source: Typical XRF spectra of MgO and quartz substrates fluoresced with Am241-Mo source are shown in figure 5.5. They consist of the usual Mo K lines produced by the source and two additional peaks produced by the Compton scattering of MoK_α and MoK_β lines. The two spectra have a very smooth and featureless background and no Mg or Si from the substrates nor Ar from the air is detected.

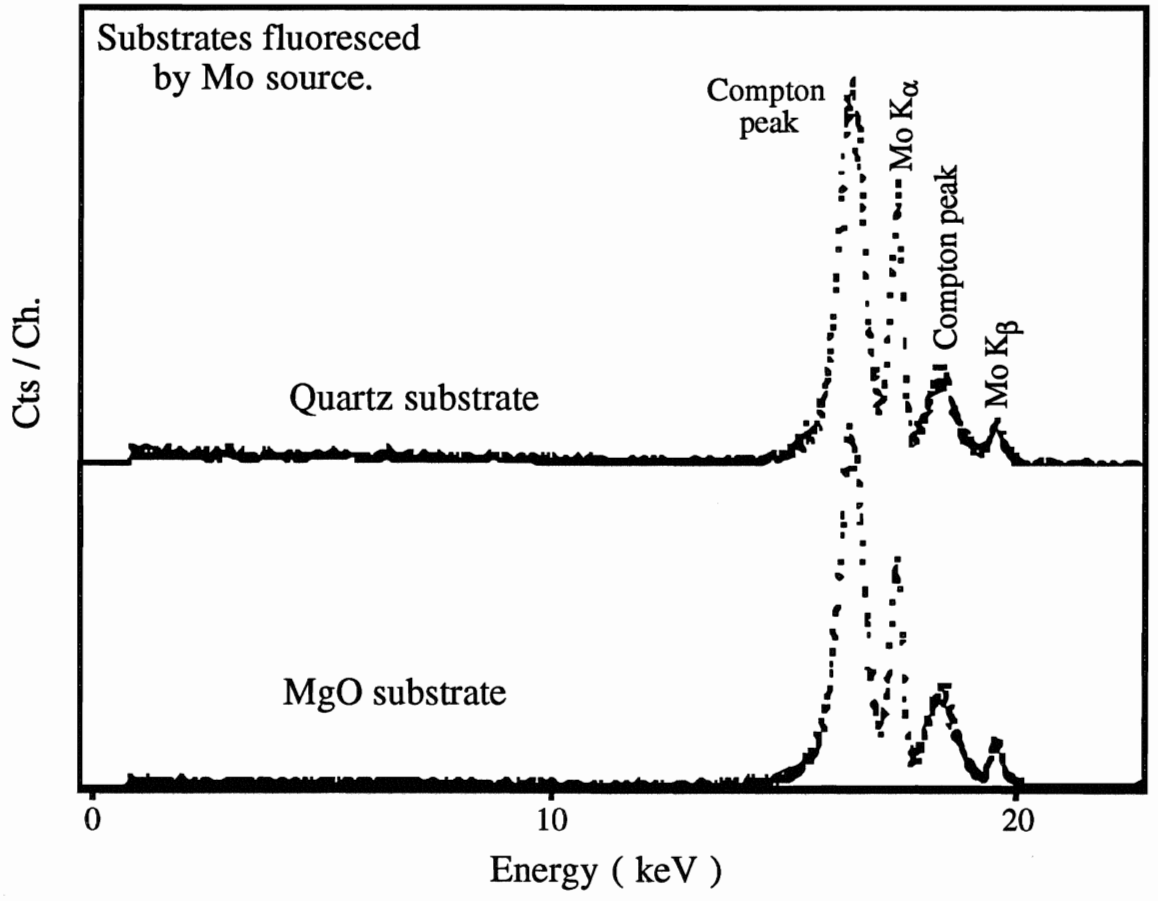

Fig. 5.5 X-ray spectra from MgO and quartz substrates.

(ii) Fe55 Source: Figure 5.6 shows the similar features of a quartz substrate fluoresced by the Fe^{55} source. It consist of Mn K_α and Mn K_β lines produced by the source. In addition to these lines the spectra have two fluorescent lines; Si K_α line from the quartz substrate and an Ar line produced from the Ar atoms in the surrounding air. This Ar line was removed by introducing nitrogen gas into the radioactive source assembly as shown in figure 3.2.

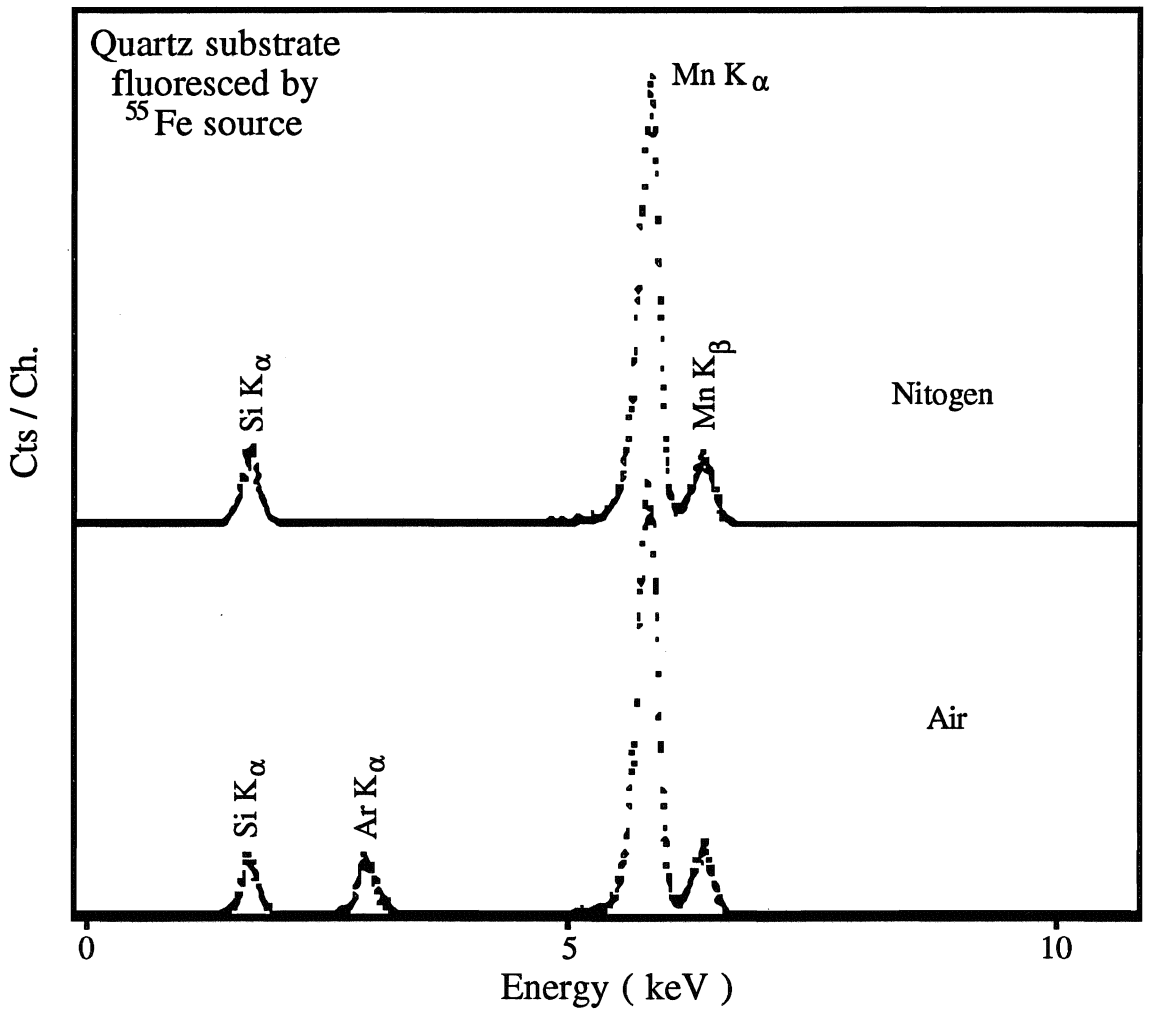

Fig. 5.6 X-ray spectra from a quartz substrate.

(5.4) Analysis of the fluorescent x-ray spectra:

The goal of this analysis is to determine the net area Y_{Net}, above the background, of the full energy peaks; it is measured as the number of counts accumulated under the peak. Consider the fluorescent x-ray spectrum of a CuSr film on a quartz substrate fluoresced with the Am241-Mo source as shown in figure 5.7. It consists of simple isolated peaks superimposed on a flat background. The region of interest for a single peak is defined by two channels, A and B, which are chosen to mark where the peak meets the background. A and B are located an equal number of channels from the center of the peak.

The total area, Y_{Tot}, of each peak is determined by adding up the counts in the region of interest, between A and B. The background of each peak, Y_{Bkg}, is the number of counts in the area of the rectangle between channels A and B with a height equal to the average number of counts per channel of three channels to the left of channel A and to the right of channel B. Therefore, the net area Y_{Net} is obtained from

$$Y_{Net} = Y_{Tot} - Y_{Bkg}$$

The statistical error of the net area is given as

$$\%\sigma(Y_{Net}) = \frac{\sqrt{(\sqrt{Y_{Tot}})^2 + (\sqrt{Y_{Bkg}})^2}}{Y_{Net}} \times 100$$

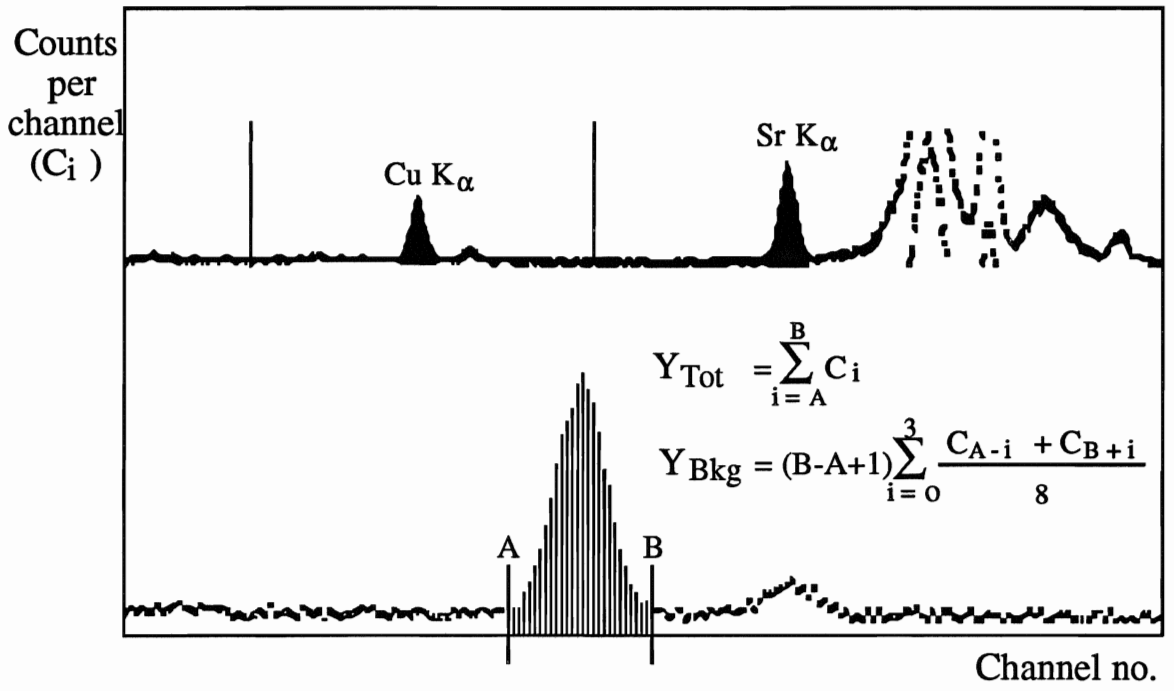

Fig. 5.7 Methods of obtaining peak areas from a multichannel spectra.

(6) Calibration of XRF system using sol gel films

(6.1) Introduction:

The calibration technique described in this section uses sol gel films which are assumed to have the same chemical compositions as the mixtures from which they were prepared by depositions on a quartz substrate. Since the sol gel films were not uniform in thickness the average value was estimated. Any film that is free of thickness dependence is suitable for use as a standard in determining the calibration constant $\mathbf{C}_{A,B}$ for thin films.

(6.2) Cu-Br sol gel films:

A typical fluorescent x-ray spectrum of Cu-Br film on quartz substrate is shown in figure 6.1 . It shows four characteristic lines (Cu Kα,Kβ and Br Kα,Kβ). Only the data for the Kα lines were analyzed. The XRF measurements of the net yield (Ynet) of Cu Kα and Br Kα lines are shown in table 5.1 with their ratios. These measurements were taken for sets of Cu-Br films made from two different compositions (Cu_1Br_1, Cu_2Br_1), counted for 1hr.

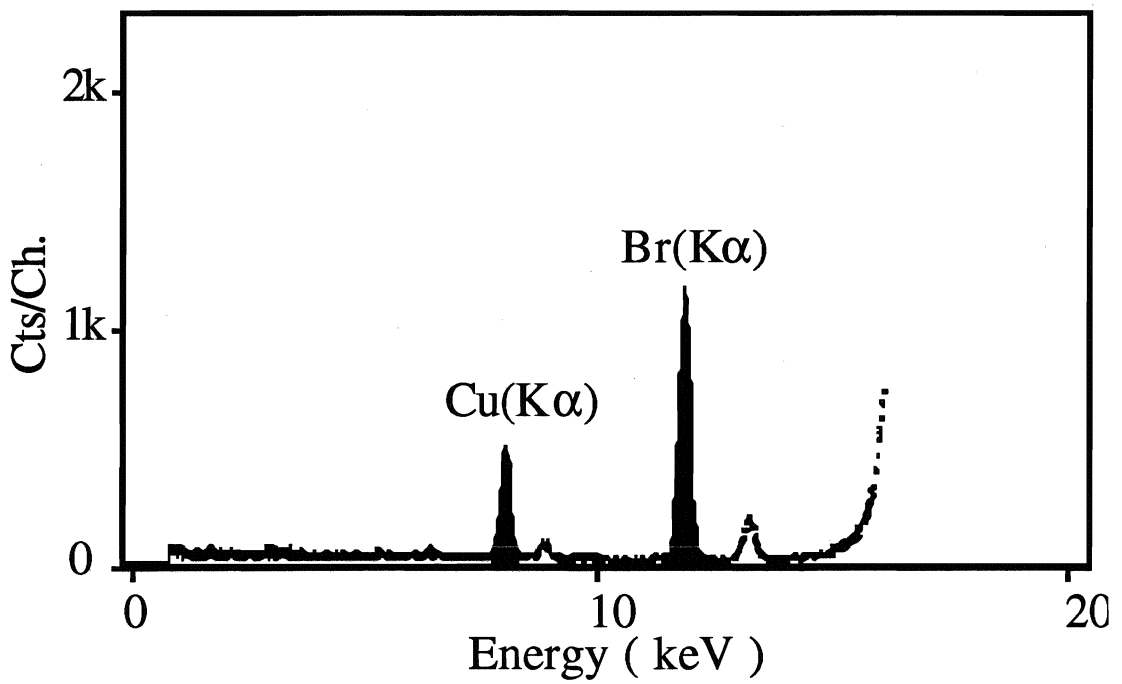

Fig. 6.1 X-ray spectrum of Cu-Br sol gel thin film.

The results of the yield ratio in table 6.1 do not indicate any systematic dependence on film thickness. The reproducibility of the solution used to make films 5.1a-5.1c was proven by the use of a replica solution to produce film 5.1d. Film 5.1a was fluoresced twice, the results of the second run are listed as run 2. The two results prove the reproducibility of the XRF measurements within the expected precision.

The average values of the calibration constant for Cu and Br ($\mathbf{C}_{Cu,Br}$) are shown in table 6.2 . This table was provided to show if there is any difference between $\mathbf{C}_{Cu,Br}$ measured from the two different film compositions. The two different film compositions gave the same $\mathbf{C}_{Cu,Br}$ within the statistical precision and there is no thickness effect evident from these results.

Table 6.1

Film composition	Film #	n_{Cu}/n_{Br}	Net YCu	Net YBr	YCu/YBr
$Cu_1 Br_1$	5.1a(0.6 μm) run 1	1	2350 ± 66	5845 ± 88	0.402±0.017
	run 2	1	2351 ± 66	5756 ± 86	0.408±0.018
	5.1c(1.1μm)	1	4759 ± 81	13165 ± 118	0.361±0.009
	5.1d(0.9μm)	1	3779 ± 76	9377 ± 103	0.403±0.013
$Cu_2 Br_1$	5.2a(0.3 μm)	2	2807 ± 81	3864 ± 81	0.726±0.036
	5.2b(2.0μm)	2	8594 ± 103	10748 ± 107	0.800±0.018

Table 6.2

Film	n_{Cu}/n_{Br}	Average $C_{Cu,Br}$	Overall Average $C_{Cu,Br}$
$Cu_1 Br_1$	1	2.55 ± 0.05	2.57 ± 0.04
$Cu_2 Br_1$	2	2.63 ± 0.08	

(6.3) CuSr sol gel films:

Three different film compositions were used to determine the calibration constant for Cu and Sr ($C_{Cu,Sr}$). Two films contain Cu and Sr only and one film contains Bi, Sr, Ca, and Cu. The fluorescent x-ray spectra of CuSr and BiSrCaCu films are shown in figures 6.2 and 6.3 respectively. Both these films were fluoresced with an ^{241}Am-Mo

radioactive source. Only the Kα characteristic lines of Cu and Sr were analyzed.

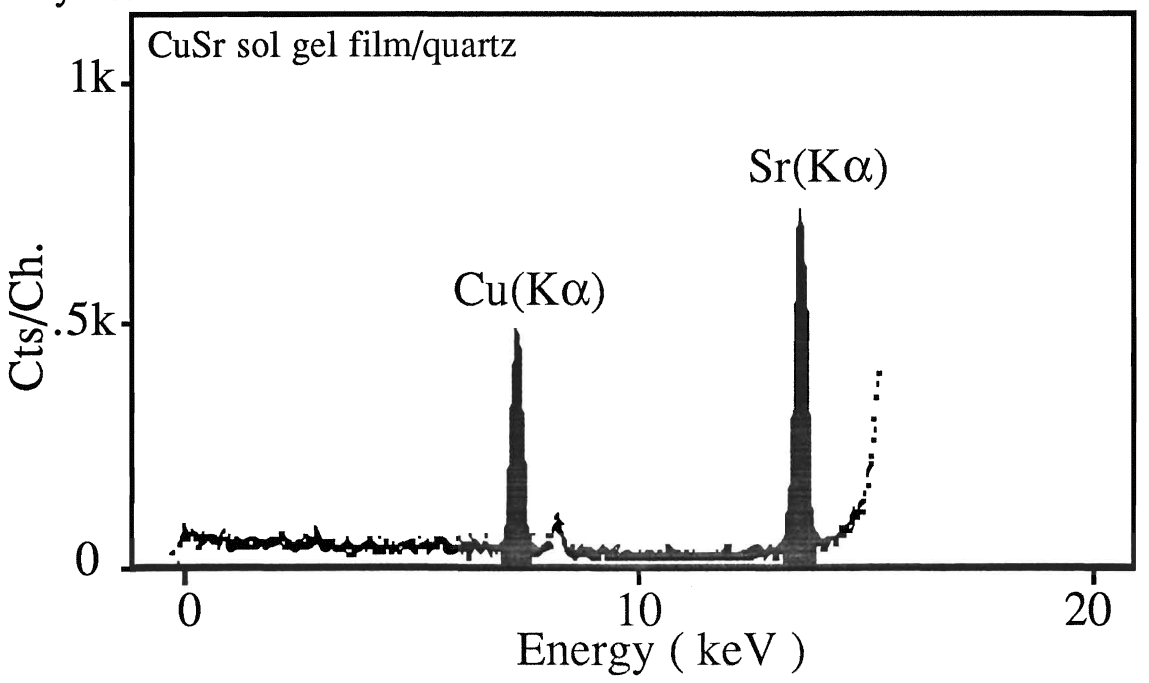

Fig. 6.2 X-ray spectrum of CuSr sol gel thin film.

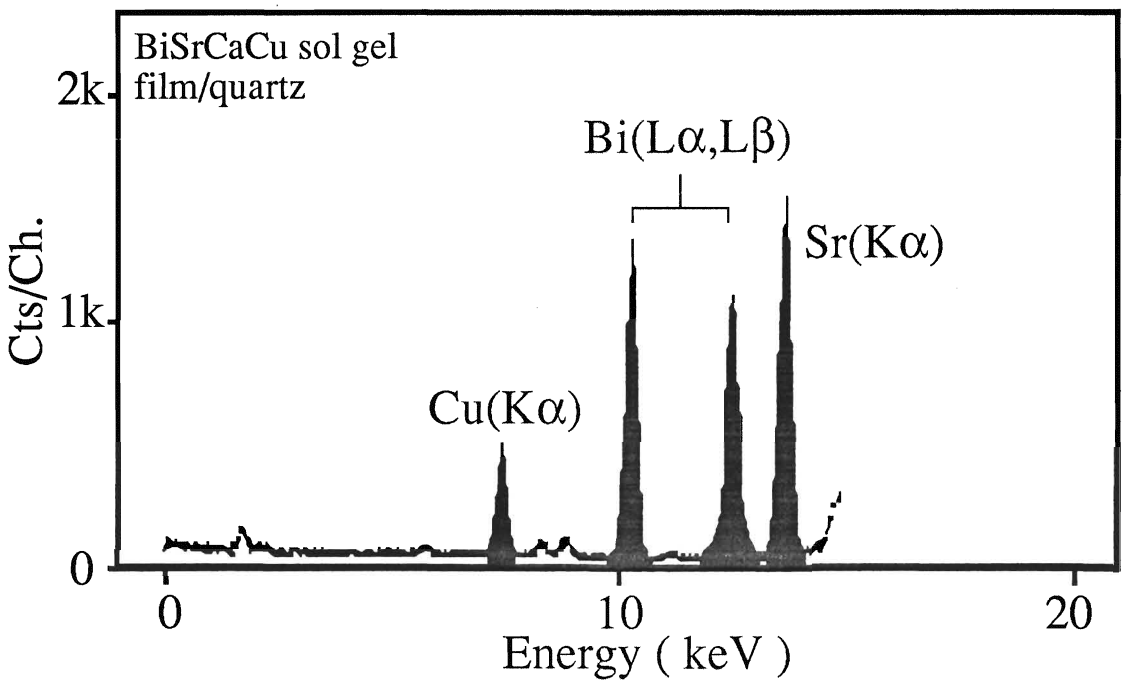

Fig. 6.3 X-ray spectrum of BiSrCaCu sol gel thin film.

Table 6.3 contains the net yield of Kα lines of Cu and Sr from the three films counted for 1hr. The results in table 6.3 do not indicate any systematic dependence on film thickness.

The results of the average values of $C_{Cu,Sr}$ are tabulated in table 6.4. The difference observed between the $C_{Cu,Sr}$ measured from the different film compositions could not be attributed to thickness effect as it was seen from table 6.3 that there is no systematic dependence on thickness. Also these differences can not be attributed to not having the right film composition because it was seen later from the yield ratios in table 6.5 that these films do have the right composition. The only error which can be attributed to these differences is due to the statistical measurements.

Table 6.3

Film composition	Film #	n_{Cu}/n_{Sr}	Net YCu	Net YSr	YCu/YSr
Cu_1Sr_1	5.3a(0.6μm)	1	2736±68	9322±112	0.293±0.011
	5.3b(2.6μm)	1	10879±109	37819±189	0.288±0.004
Cu_2Sr_1	5.4a(0.6μm)	2	5240±84	9398±113	0.558±0.016
	5.4b(0.6μm)	2	5159±83	8802±106	0.586±0.016
	5.4c(1.6μm)	2	6959±97	12302±123	0.566±0.014
$Bi_2Sr_2CaCu_2$ on quartz	5.7a(.24μm)	1	1975±73	7337±110	0.269±0.014
$Bi_2Sr_2CaCu_2$ on MgO	5.7b(1.1μm)	1	4841±82	18281±146	0.265±0.007

Table 6.4

Film composition	n_{Cu}/n_{Sr}	Average $C_{Cu,Sr}$	Overall Average $C_{Cu,Sr}$
$Cu_1 Sr_1$	1	3.44±0.07	3.56±0.04
$Cu_2 Sr_1$	2	3.51±0.05	
$Bi_2Sr_2Ca_1Cu_2$	1	3.75±0.11	

(6.4) CuBi sol gel films:

The calibration constant for Cu and Bi ($C_{Cu,Bi}$) was calculated similarly as before. For Bi, however, the measurements of both Lα, and Lβ were analyzed (see figure 6.4 for CuBi film). Table 6.5 contains the XRF measurements of the net yield of Cu Kα lines and the sum of the Lα and Lβ with their ratios counted for 1hr. Again, here, there is no dependence on thickness evident from these results. The fact that yield ratios were doubled when the film composition, n_{Cu}/n_{Bi}, was changed from one to two indicates that the assumption made in the beginning for films having the right composition is valid.

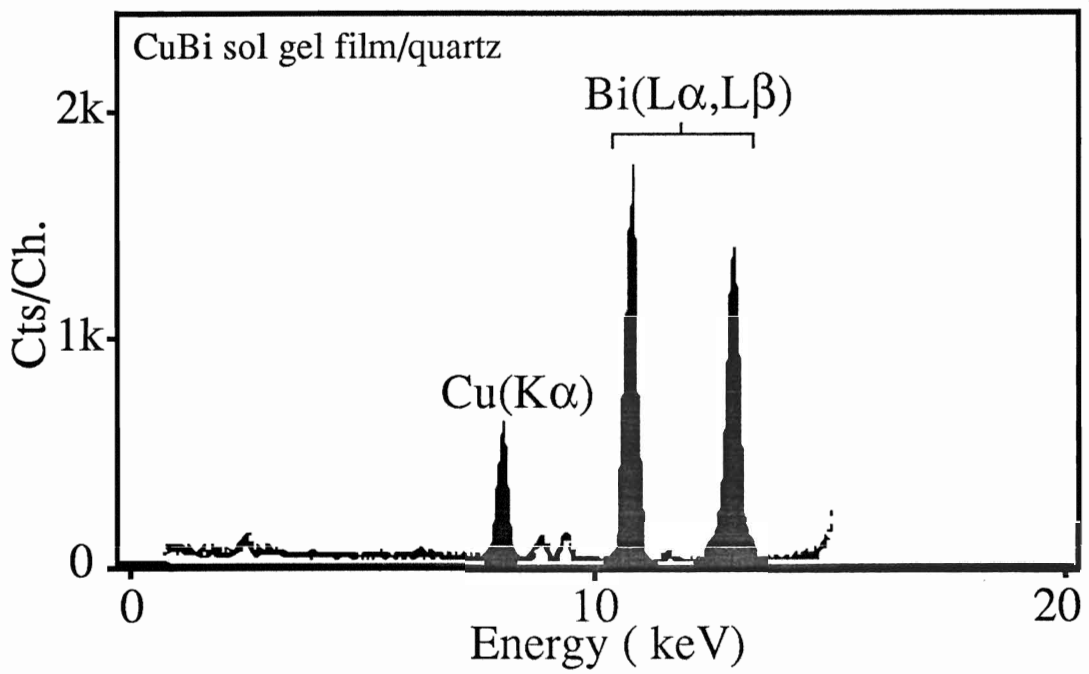

Fig. 6.4 X-ray spectrum of CuBi sol gel thin film.

The average values of $C_{Cu,Bi}$ are tabulated in table 6.6. They are in agreement with each other within the statistical precision.

Table 6.5

Film	Film #	Expected n_{Cu}/n_{Bi}	Net YCu	Net YBi	YCu/YBi
Bi_1Cu_1	5.5a(0.2μm)	1	1501±69	9473±376	0.158±0.014
	5.5b(0.9μm)	1	3731±78	24480±490	0.152±0.006
	5.5c(1.4μm)	1	5982±90	38311±613	0.156±0.005
Bi_1Cu_2	5.6(0.24μm)	2	2186±78	7134±359	0.306±0.026
$Bi_2Sr_2CaCu_2$ on quartz	5.7a(.24μm)	1	1975±73	12796±422	0.154±0.011
$Bi_2Sr_2CaCu_2$ on MgO	5.7b(1.1μm)	1	4841±82	31329±564	0.155±0.005

Table 6.6

Film composition	n_{Cu}/n_{Bi}	Average $C_{Cu,Bi}$	Overall Average $C_{Cu,Bi}$
Bi_1Cu_1	1	6.44±0.21	6.47±0.17
Bi_1Cu_2	2	6.54±0.56	
$Bi_2Sr_2Ca_1Cu_2$	1	6.47±0.25	

(7) Calibration of XRF system using sputtered films of known composition as determined by RBS

(7.1) Introduction:

This section describes the calibration of the XRF system using sputtered films of known composition as determined by the well established method, RBS. Three different sputtered films SrCaCuO, BiCaCuO, and BiSrCaCuO were prepared from sintered targets of nominal composition of $Sr_1Ca_1Cu_1O_x$, $Bi_1Ca_1Cu_3O_x$, and $Bi_2Sr_2Ca_1Cu_2O_x$ respectively. The thickness of the films (~1500Å) was chosen to give the simplest possible RBS spectrum consisting of separate peaks for the different elements.

(7.2) Composition measurements using RBS:

RBS is a widely used method for the non-destructive determination of the composition of thin films and the analysis is simple and quantitative. Monoenergetic particles (MeV He ions) in the incident beam collide with target nuclei and are scattered backward into a detector. Measurements of the intensity and energy of the scattered particles provides a direct measure of elemental composition.

Figure 7.1 shows a typical backscattering geometry. Particles scattered from the surface atoms have an energy given by $E_1 = KE_0$, where K (the kinematic factor) is a function of M_1, M_2 and θ. This shows that the energy after scattering is determined by the mass of the particle target atom and the scattering angle. The incident particles lose energy in penetrating the target along the incident path (ΔE_{in}), in the elastic scattering process (ΔE_s), and along the exit path (ΔE_{out}). Therefore the energy of a particle scattered from a depth t is given by [10,14]

$$E'_1 = E_0 - \Delta E_{in} - \Delta E_s - \Delta E_{out}$$

where $\Delta E_s = (1 - K)(E_0 - \Delta E_{in})$

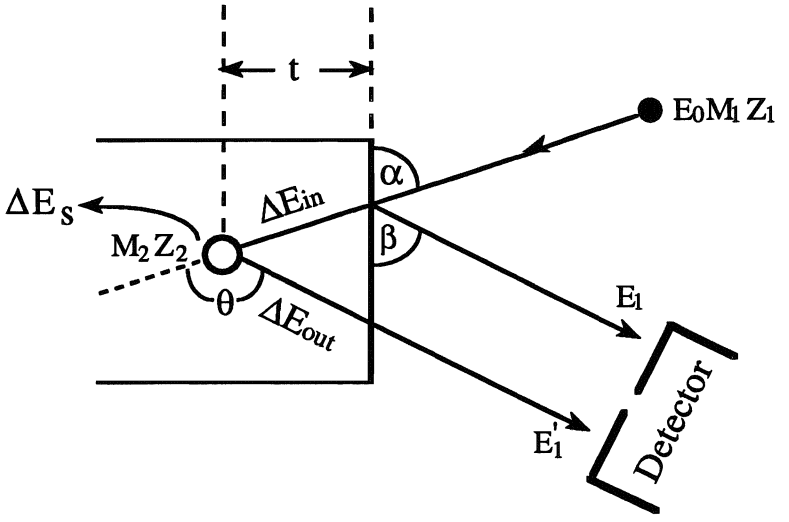

Fig. 7.1 Schematic illustration of the parameters of RBS.

An actual backscattering spectrum (θ=170°) for 2.9MeV He^{++} ions incident on SrCaCuO thin film taken at the University of Western Ontario is shown in figure 7.2. The area,Λ , the total number of counts integrated through each peak in figure 7.2 is given by [10,16]

$$\Lambda = \sigma \Omega Q N \Delta t \qquad (7.1)$$

where Δt is the effective path length.

Ω is the detector solid angle (steradian).

Q is the number of the incident particles in the beam.

σ is the differential scattering cross section (cm^2 per steradian).

N is the number of target atoms per cm^3 .

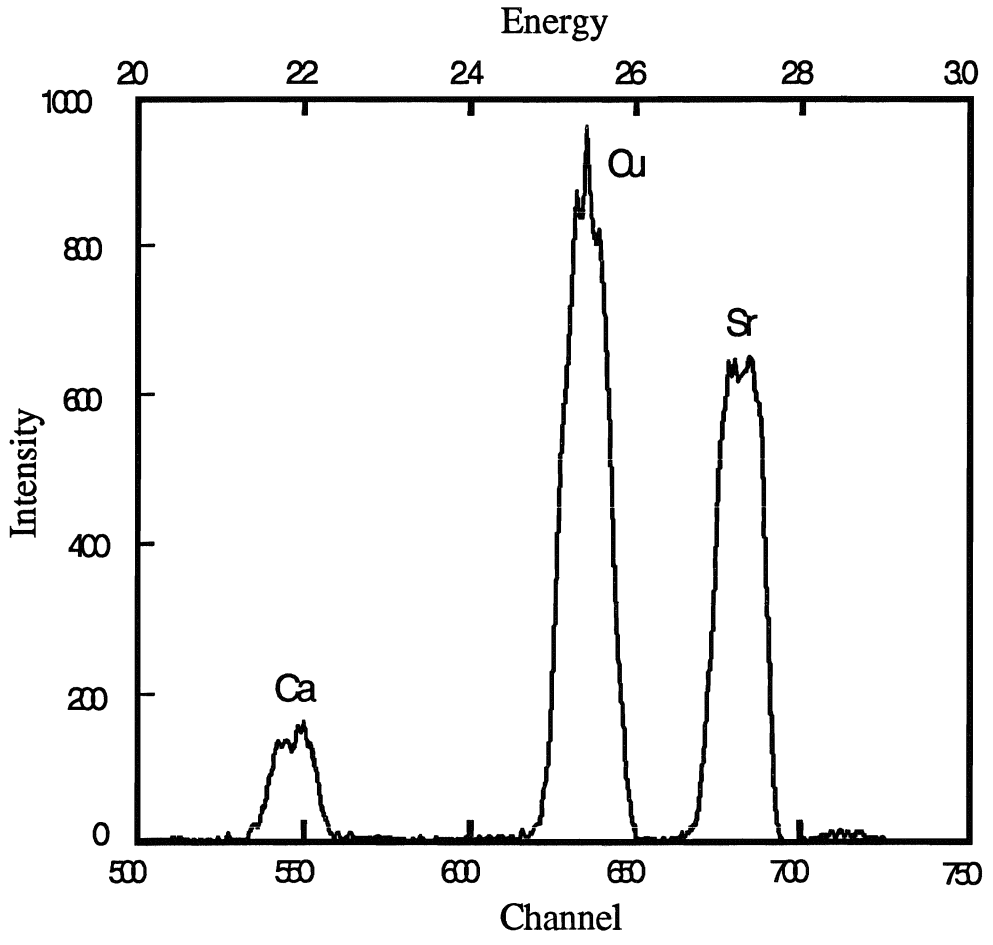

Fig. 7.2 RBS energy spectrum obtained with 2.9MeV He^{++} ions from SrCaCuO thin film on MgO substrate.

Therefore the concentration ratio of two elements A and B is

$$\frac{N_A}{N_B} = \frac{\Lambda_A}{\Lambda_B}\frac{\sigma_B}{\sigma_A} \tag{7.2}$$

and since the scattering cross section is proportional to Z^2, then

$$\frac{N_A}{N_B} = \frac{\Lambda_A}{\Lambda_B}\left(\frac{Z_B}{Z_A}\right)^2 \tag{7.3}$$

The area of the RBS peaks and the XRF yields of the three sputtered films are tabulated in tables 7.1 and 7.2 respectively. The Cu, Sr, and Bi XRF yields were measured using Am241-Mo radioactive source and the Ca yields using the ^{55}Fe source. Thus, the XRF calibration constant was calculated for these films from composition as measured by RBS and the XRF yields. The calibration constant $C_{A,B}$ is tabulated in table 7.3

Table 7.1

1	2	3	4	5	6	7
	RBS MEASUREMENTS					
Line	He^{++} Beam	Film	Λ_{Cu}	Λ_{Sr}	Λ_{Bi}	Λ_{Ca}
1	2.9MeV	SrCaCuO	34178±602	25390±528	-----	5258±252
2	4.0MeV		13970±120	10270±102	-----	2130±50
3	2.9MeV	BiCaCuO	19282±476	-----	248600±1616	2355±85
4	4.0MeV		7780±95	-----	99880±319	-----
5	4.0MeV	BiSrCaCuO	16671±142	27676±173	94730±314	-----

Table 7.2

3	8	9	10	11
	XRF MEASUREMENTS			
Film	net Y_{Cu}	net Y_{Sr}	net Y_{Bi}	net Y_{Ca}
SrCaCuO	7062±113	11103±144	-----	33217±249
BiCaCuO	2590±80	-----	25985±543	9799±156
BiSrCaCuO	2096±65	7152±100	9569±344	8007±137

Table 7.3

1	12	13	14	15	16
Line	$C_{A,B}$ Calculations from sputtered films				
	Elements		$\frac{N_A}{N_B} = \frac{\Lambda_A}{\Lambda_B}\left(\frac{Z_B}{Z_A}\right)^2$	$C_{A,B} = \frac{N_A/N_B}{Y_A/Y_B}$	Average $C_{A,B}$
	A	B			
1	Cu	Sr	2.311±0.089	3.63±0.16	3.61±0.10
2			2.336±0.043	3.67±0.11	
5			1.034±0.015	3.53±0.21	
3	Cu	Bi	0.635±0.020	6.37±0.53	6.45±0.29
4			0.638±0.010	6.40±0.43	
5			1.442±0.017	6.58±0.52	
1	Cu	Ca	3.092±0.203	14.54±1.30	14.65±0.74
2			3.119±0.100	14.67±0.82	
3			3.894±0.237	14.73±1.59	
1	Sr	Ca	1.338±0.092	4.00±0.36	4.00±0.21
2			1.336±0.045	4.00±0.22	

The three independent measurements for $C_{Cu,Sr}$, are in excellent agreement. Similarly for the other calibration constants. These results do not indicate any systematic difference in constants which can be related to thickness effect. The results for $C_{Cu,Ca}$ are obtained from two independent sputtered films and agree with each other in the limit of the statistical precision. This is true also for $C_{Cu,Sr}$ and $C_{Cu,Bi}$.

On the other hand only two measurements obtained for $C_{Sr,Ca}$ from one film and it is acceptable as long as the film is considered to be thin. To double check this a computer simulation was done to the SrCaCuO film to determine the effective thickness and the atomic density of the film. By choosing the density to be $6x10^{22}$ atoms/cm^3, the simulation gave an effective thickness of 1500Å. Hence, from equation 2.8 one can estimate the secondary fluorescence (S_{Sr}, S_{Cu}, and S_{Ca}) and absorption (a_{Sr}, a_{Cu}, and a_{Ca}) contribution { i.e. $\frac{(1 + S_B)}{(1 + S_A)} \frac{a_B}{a_A}$ } and it was found to be 0.96 for $\frac{n_{Cu}}{n_{Sr}}$ and 0.99 for $\frac{n_{Sr}}{n_{Ca}}$.

where S_{Sr} and S_{Ca} equal to zero and $S_{Cu} = 0.0458$

$a_{Sr} = 1.496x10^{-5}$, $a_{Ca} = 1.480x10^{-5}$, and $a_{Cu.} = 1.495x10^{-5}$ cm.

This is another independent way to show that the film is considered to be thin. Also the product of $C_{Sr,Ca}$ x $C_{Cu,Sr}$ (=14.44) should have the same value as for $C_{Cu,Ca}$ (=14.65), which is the same within the measured errors. This is again another independent way to check for thickness effect.

The results of the calibration constants $C_{A,B}$ for some elements independent of thickness obtained from standards of sol gel films, sputtered-RBS films, and from the theoretical calculations are shown in table 7.4. The results of $C_{Cu,Bi}$ $C_{Cu,Sr}$ from the sputtered films and the sol gel films in table 7.4 are in agreement with each other within the estimated errors. For the case of Ca and Br measurements, results for $C_{Cu,Ca}$, $C_{Sr,Ca}$, and $C_{Cu,Br}$ are obtained only from one calibration

method.

The agreement between the results of the two experimental methods and the theoretical calculations from chapter 2 table 2.3 lead to the conclusion that either calibration technique is satisfactory and although the calibration technique is different, the constants are independent of film composition in the limit of thin films.

The error figures of the constants include the uncertainty in the RBS and XRF yields. These errors could have been reduced had the yields been measured for longer time to improve the statistical precision.

Table 7.4

Elements		$C_{A,B}$		
A	B	Sol gel	Sputtered-RBS	Calculated
Cu	Br	2.57±0.04	-----	2.56
Cu	Sr	3.56±0.04	3.61±0.10	3.63
Cu	Bi	6.47±0.17	6.45±0.29	-----
Cu	Ca	-----	14.65±0.74	-----
Sr	Ca	-----	4.00±0.21	-----

(8) Application of XRF to Sputtered films

(8.1) Introduction:

The XRF method of determining the composition described previously has proved to be very useful for checking the reproducibility of sputtered films under certain conditions and for evaluating the effects of various sputtering parameters such as substrate-to-target distance, substrate temperature and eventually target structure and composition on the gross composition of the sputtered films.

(8.2) Stability of the Sputtering Machine:

It was very essential to ensure that the sputtering machine can produce films with the same composition if all parameters such as gas pressure and sputtering power are kept fixed. An extensive series of measurements on sputtered films was made in the beginning. All the sputtering machine targets which were used were sintered targets with nominal composition $Bi_2Sr_2Ca_1Cu_2O_x$. The maximum power these targets can take was found to be 20 Watts otherwise arcing starts. It was found that the effect of increasing sputtering power is to increase the film growth rate. The gas pressure was kept at Ar/O_2 20/10 mTorr. Table (8.1) shows some representative XRF results of the sputtered films produced before [8.1a), b), c)] and after [8.1d), e)] establishing the reproducibility of operation of the sputtering machine.

Table 8.1

Film #	Thickness	Y_{Cu}/Y_{Bi}	Y_{Cu}/Y_{Sr}
8.1a	0.7kÅ	0.124±0.018	0.499±0.068
8.1b	4kÅ	0.092±0.003	0.352±0.013
8.1c	3.8kÅ	0.072±0.002	0.445±0.015
8.1d	1.8kÅ	0.084±0.007	0.425±0.033
8.1e	2.7kÅ	0.084±0.004	0.425±0.019

The results of the table (8.1) illustrate the improved reliability of the sputtering machine to produce films with the same composition. Due to preferential sputtering, however, the composition of the films may not be the same as the target material. This is the case for the film data in tables 8.1, 8.2 and 8.3. It is evident that films 8.1a - 8.1c gave different results which was eventually found to be due to some leakage in the sputtering machine and a problem in the pressure gauges. After all the problems were found and fixed, XRF measurements showed that the sputtering machine operated reproducibly to produce films with the same composition, see film 8.1d and 8.1e.

(8.3) Optimizing Target Composition and Other Parameters:

Up to this stage all the targets were sintered targets with nominal composition $Bi_2Sr_2Ca_1Cu_2O_x$ and the substrate-to-target distance was kept fixed at 22cm. This combination of parameters has some disadvantages: (1) it takes about 20 - 22 hr to sputter a film with thickness

of ~ 3000Å, (2) the target can not be used again if it is sputtered for that time, and (3) it takes about 5 days to make a sintered target. Therefore, it was necessary to find a way to increase the process of sputtering. Hence, the substrate-to-target distance was decreased to 12cm and new targets were prepared by melt-casting the powder in a copper mold. These targets were found to take more power and last longer than sintered ones, hence, the sputtering time is less and the film growth rate increases.

XRF measurements were used to show that the initial melt cast targets had different composition at the surface and in the bulk. This was done by x-raying the surface of the unaltered target, then the target was cut in half and the interior was x-rayed. The targets were heated at 750°c to make them homogeneous and to reduce their thermal resistivity. Table (8.2) gives representative XRF results which shows the difference between films produced from sintered target and melt-cast target with nominal composition $Bi_2Sr_2Ca_1Cu_2O_x$.

Table 8.2

Film #	Target	Y_{Cu}/Y_{Bi}	Y_{Cu}/Y_{Sr}
8.2a	Sintered	0.089±0.002	0.465±0.012
8.2b	Melt-cast	0.063±0.002	0.411±0.016

The new melt-cast targets are very easy to make which enables us to change the composition very easily to produce films with the desired composition. Various targets with different composition were made, but the results for only three targets will be discussed here. Table (8.3) shows the results of sputtered films produced from three different melt-cast targets and different substrate temperature.

Table 8.3

Target no.	Target Compositions			
	Bi	Sr	Ca	Cu
A	2	2	1	0.6
B	2	1.88	0.94	1.43
C	2	1.88	1.69	1.43

Target	Film#	Sub.temp °C	Film composition		
			$\frac{n_{Cu}}{n_{Bi}}$	$\frac{n_{Cu}}{n_{Sr}}$	$\frac{n_{Ca}}{n_{Cu}}$
A	D12	730	0.36±0.03	0.36±0.02	-----
B	D23	700	1.05±0.14	0.91±0.08	-----
	J3	650	0.80±0.09	1.48±0.12	-----
	annealed		0.80±0.09	1.43±0.12	-----
	J2	~ 730	1.41±0.16	1.06±0.07	0.26±0.03
	J6	670	0.97±0.10	1.31±0.10	0.25±0.03
C	M21	---	0.69±0.06	1.07±0.06	0.47±0.04
	annealed	---	0.72±0.06	1.08±0.06	0.41±0.03
	M20	---	1.21±0.10	1.07±0.06	0.36±0.03

The XRF method of determining the composition using the calibration constants was particularly useful for evaluating the effects of various sputtering parameters such as target composition and substrate temperature on the gross composition of the thin films. It should be mentioned here that there was no total control of the substrate temperature due to instrumental problems. The results of table 8.3 illustrate the improvements of the thin film composition by changing these parameters.

The first optimization measurements were done only for the content of Bi and Sr relative to the Cu. and that can be seen from the first four entries of table 8.3. After the XRF was calibrated for Ca , the Ca content was measured and target B was found to produce film with deficiency in Ca. However target B proved to produce films with the expected composition of Bi, Sr, and Cu (i.e. Bi_1, Sr_1, and Cu_1) as can be seen from film D23. None of the films produced from target B or prior to that showed any sign of superconductivity.

Therefore the XRF was particularly useful for predicting the amount of Ca which leads us to alter the target composition by increasing the amount of Ca in target C. Because of the enrichment of Ca in target C, superconducting films with the desired phase (2212) were obtained. For example, film M20 gave two transitions one at 112K and zero resistance at 76K after post annealing in air as shown in figure 8.1. Also the XRF demonstrated that post annealing of the film, which is necessary to produce high T_c thin films, has no affect on Bi, Sr, Ca, and Cu. This can be seen from the results of post annealing of films J3 and M21.

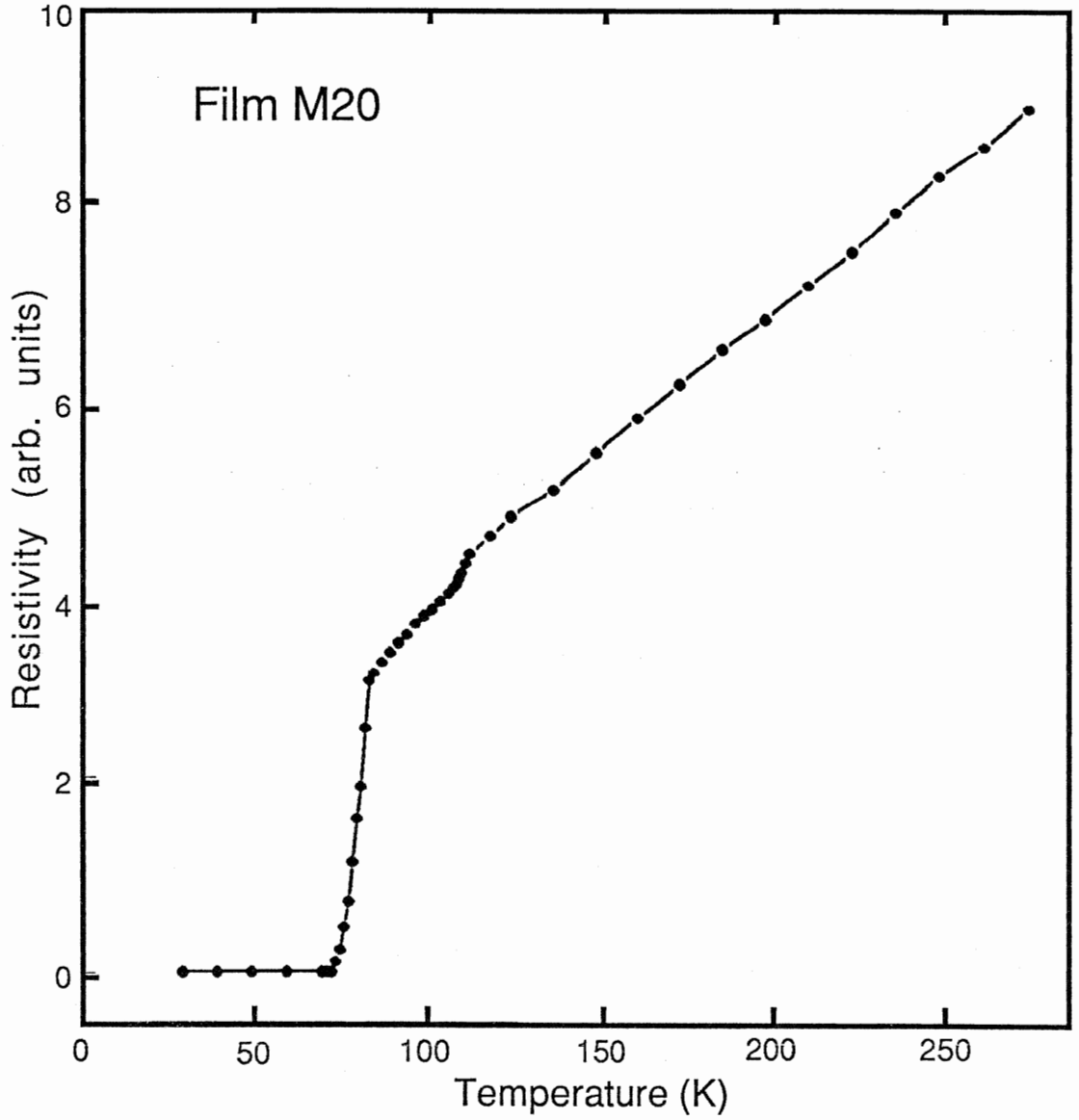

Fig. 8.1 Resistivity measurements of film M20 annealed in air.

(9) Summary and Conclusion

It has been successfully shown that the XRF system assembled at Brock University is capable of providing reliable and accurate determination of the stoichiometry of thin films. The system has been calibrated for Ca, Cu, Br, Sr (K x-rays), and Bi (L x-rays).

The methods used for calibrating the XRF system required (a) the preparation of sputtered thin films. (b) the preparation of sol gel thin films. (c) the use of the RBS technique for analyzing the sputtered films.

The results of the measurement of the thin film XRF calibration constant, $C_{A,B}$, obtained by using sol gel films and sputtered-RBS films are in excellent agreement with each other and with the simple theoretical calculation using the fluorescent K x-ray atomic data (table 7.4). The results of the theoretical calculations using the L x-ray atomic data available did not give reliable results. The calibration results show that (i) either sol gel or sputtered-RBS films are suitable for calibrating the system. (ii) it suggests that the same calibration constant can be obtained from different films regardless of film composition. (iii) if calibrated films containing the elements of interest are difficult to prepare then a theoretical value for the XRF calibration constant may be calculated and used, in certain cases. We have shown that correct (that is, in agreement with experiment) theoretical values may be calculated for those elements whose K x-ray energies are in the range from ~6-20keV, since this range corresponds to a known detector efficiency of 100% and absorption along the air path from film to the detector is negligible. The L x-ray atomic data [11], [14], [19] available to us did not permit sufficiently accurate

theoretical calculation to be done. (iv) the results from the very simple XRF apparatus agree with those obtained from the more sophisticated RBS system.

Theoretical estimates have been made for absorption and secondary fluorescence effects in a film. It was feasible to create from the beginning a theory capable of estimating the significance of these effects. The effects in the sputtered-RBS films used for calibrating were shown to be small enough to be ignored. The total composition and the mass of the sol gel films were not known and so no theoretical estimation was made. However from the experimental results it can be seen that there is no contribution evident from these effects.

With the calibration method described, it is easy to prepare different standards and quickly calculate a calibration constant for certain elements. The calibrated XRF system was used to measure the composition of sputtered BiSrCaCuO films. In particular, it was used to determine the sputtering target and operating parameters that were required to prepare superconducting films. Since the determination of the stoichiometry was accurate and non-destructive, other physical properties were measured. Other significant results of this work is that it was useful to assist and monitor the production of high-T_c thin films. Unfortunately the determination of the oxygen content using this method could not be done.

The application of the XRF system to determine other elements in thin films would require the preparation of additional standard films for calibration.

References

1. L. I. Maissel and M. H. Francombe, "An Introduction To Thin Films", Science Publishers Inc., New York (1973).

2. L. Eckertova, "Physics of Thin Films", 2nd ed., Plenum Press, New York (1986) p 148-196, 202-292

3. N. G. Dhere, in "Physics of Thin Films", ed. by M. H. Francombe and J. L. Vossen, Academic Press Inc., San Diego **16** (1992) p 101-123.

4. L. C. Feldman and J. W. Mayer, "Fundamentals of Surface and Thin Film Analysis", Elsevier Science Publishing Company Inc., New York (1986) p 13-66, 81-87, 257-262.

5. A. Zangwill, "Physics At Surfaces", Cambridge University Press, New York (1988) p. 24-26.

6. J. S. Williams, J.R. Bird, M. J. Kenny, and J. E. E. Baglin, in "Ion Beams for Materials Analysis", ed. by J. R. Bird and J. S. Williams, Academic Press, Sydney (1989) p 3-148.

7. R. Woldseth, "X-Ray Energy Spectrometry", Kevex Corporation, Burliname, California (1973).

8. J.-B. Cheng, Y.-Z. Zhao, and B.-R. Zhao, Appl. Spec. **44** (1990) 826.

9. L. Bergel and F. J. Cadieu, X-Ray Spectrom. **9** (1980) 19.

10. R. Eisberg and R. Resnik, "Quantum Physics of Atoms, Molecules, Solids, Nuclei, and particles",2nd.ed., John Wiley and Sons, New York (1985) p 26-51, 337-342.

11. J. W. Mayer and E. Rimini, "Ion Beam Handbook for Material Analysis", Academic Press, New York (1977).

12. B. D. Cullity, "Elements of X-Ray Diffraction", Addisn-Wesley Publishing Company Inc., Reading, Massachusetts (1978) p 3-30.

13. D. Berenyi, P. Chevallier, in "X-Ray Spectroscopy in Atomic and Solid State Physics", ed. by J. G. Ferreira and M. T. Ramos, Plenum Press, New York (1988) p 25-29, 237-550.

14. W. H. McMaster, N. K. D. Grande, J.H. Mallett, and J. H. Hubbell, "Compilation of X-ray Cross Sections", Lawrence Radiation Laboratory Report, UCRL-50174 (May 1969).

15. R. M. Eisberg, "Fundamentals of Modern Physics", John Wiley and Sons, New York (1961) p 505-512.

16. T. N. Blanton, C. L. Barnes, and M. Lelental, Physica C 173 (1991) 152.

17. C. Bhan, S. N. Chaturvedi, and N. Nath, X-Ray Spectrom. **10** (1981) 128.

18. C. G. Lagarde, A. Pape, D. Tenorio, C. Zarate, M. Menu, L. Scotee, A. Jaidar, R. Alviso, D. Gonzalez, and V. Gonzalez, Nucl. Instr. and Meth. in Physics Research **98** (1986) 93

19. J. H. Scofield, Phys. Rev. **9** (1974) 1041.

20. E. G. and G. Ortec, "Nuclear Instruments : Systems, Radiation Detection, Measurments, and Analysis", Oak Ridge.

21. K. Debertin and R. G. Helmer, " Gamma- and X-Ray Spectrometr with Semiconductor Dectors", Elsevier Science Publishers B. V., Amsterdam (1988).

22. Y. Mei, L. Luo, and R. Hu, Appl. Phys. Lett. **56** (1990) 581.

23. H. U. Habermeier, W. Sommer, and G. Martens, J. Appl. Phys. **65** (1989) 2549.

24. C. R. Guarnieri, R. A. Roy, K. L. Saenger, S. A. Shivashankar, D. S. Yee, and J. J. Cuomo, Appl. Phys. Lett. **53** (1988) 532.

25. A. A. Hussain and M. Sayer, J. Appl. Phys. **70** (1991) 1580.

26. C. J. Brinker and G. W. Scherer, "Sol-Gel Science : The Physics and Chemistry of Sol-Gel Processing", Academic Press, Boston (1990) p.

27. V. Slusarenko, K. R. Thampi, and J. Kiwi, J. Solid State Chem. **79** (1989) 277.